ASSESSMENT OF THE EFFECTIVENESS OF STEEL FIBRE REINFORCEMENT FOR THE PUNCHING RESISTANCE OF FLAT SLABS BY EXPERIMENTAL RESEARCH AND DESIGN APPROACH

Joaquim A.O. Barros [a], Bernardo N. Moraes Neto [b], Guilherme S.S.A. Melo [c], Cristina M.V. Frazão [d]

[a/d] University of Minho, ISISE, Dep. Civil Eng., School of Eng., Campus Azurém, Guimarães, Portugal, barros@civil.uminho.pt [a] / frazao_cristina@hotmail.com [d]

[b] University of Minho/University of Brasília-UnB, Dep. Civil Eng., School of Eng., Guimarães, Portugal, bnmn@hotmail.com

[c] University of Brasília-UnB, Dep. Civil Eng., Campus Darcy Ribeiro, Brazilia, Brazil, melog@unb.br

Abstract

The present paper deals with the experimental assessment of the effectiveness of steel fibre reinforcement in terms of punching resistance of centrically loaded flat slabs, and to the development of an analytical model capable of predicting the punching behaviour of this type of structures. For this purpose, eight slabs of 2550 x 2550 x 150 mm^3 dimensions were tested up to failure, by investigating the influence of the content of steel fibres (0, 60, 75 and 90 kg/m^3) and concrete strength class (50 and 70 MPa). Two reference slabs without fibre reinforcement, one for each concrete strength class, and one slab for each fibre content and each strength class compose the experimental program. All slabs were flexurally reinforced with a grid of ribbed steel bars in a percentage to assure punching failure mode for the reference slabs. Hooked ends steel fibres provided the unique shear reinforcement. The results have revealed that steel fibres are very effective in converting brittle punching failure into ductile flexural failure, by increasing both the ultimate load and deflection, as long as adequate fibre reinforcement is assured. An analytical model was developed based on the most recent concepts proposed by the fib Mode Code 2010 for predicting the punching resistance of flat slabs and for the characterization of the behaviour of fibre reinforced concrete. The most refined version of this model was capable of predicting the punching resistance of the tested slabs with excellent accuracy and coefficient of variation of about 5%.

Keywords: Discontinuous reinforcement; Strength; Analytical modelling; Mechanical testing

1. INTRODUCTION

The constructive system composed of flat reinforced concrete (RC) slabs supported on RC columns is the most competitive for residential and commercial buildings with span length between columns varying from 7.0 to 9.0 meters and a live load not exceeding 5 kN/m^2 [1,2]. In spite of the economic advantages of this type of slabs, several dramatic disasters have occurred due to the punching failure [3]. In fact punching can trigger the progressive collapse of the slabs, resulting in a total collapse of a building. Therefore, the punching phenomenon has attracted the attention of several researchers, and several scientific and technical papers have been dedicated to the execution of experimental programs and to the development of analytical and numerical models for a better understanding of this subject.

The available research on this topic shows that the punching resistance of flat RC slabs can be improved by using high strength concrete (HSC) [4], shear reinforcement [5,6], and discrete fibres, specially steel fibres [7-9]. With respect to the use of HSC it was demonstrated that the punching resistance increases with the concrete compressive strength. However, Maghsoudi and Sharifi [4] have also evidenced that the brittleness of the failure mode of the slab-column connection also increases with the compressive strength, which can be justified by the smaller aggregate interlock caused by the fact that the shear failure crosses the aggregates, leading to a smooth fracture surfaces. Therefore, the use of HSC can be contra-productive, unless supplementary measures are adopted to prevent the formation of shear cracks, like shear reinforcement or fibres.

In fact, as demonstrated by Melo *et al.* [5] and Choi *et al.* [6], a suitable disposition of shear reinforcement in the critical punching region of the slab can avoid the formation of punching failure mode, and can assure a ductile behaviour of the slab-column connection. However, in zones densely reinforced in bending the application of shear reinforcement can be problematic and has significant costs. Furthermore, the aimed anchorage conditions for this shear reinforcement are sometimes difficult of assuring.

Steel fibres are distributed randomly during the concrete mixing phase, like a slender type aggregate, and can be a competitive shear reinforcement solution for flat slabs since almost no costs are required to the preparation and installation of this reinforcement. However, the type and content of steel fibres, and the mixing and placing technology adopted for the steel fibre reinforced concrete (SFRC) have considerable influence of the fibre reinforcement effectiveness in terms of avoiding the occurrence of punching failure mode. In fact, fibres and surrounding matrix should be selected in order to assure fibre pullout failure mode for an effective energy absorption capacity of this composite material. Since steel fibres are the component of the concrete composition of highest mass density, a tendency for an increase of fibre content from the top to the bottom surface of the slab has been reported [10]. This tendency increases when using powerful vibration procedures. To minimize this effect, in the present work a steel fibre reinforced self-compacting concrete (SFRSCC) was developed and characterized from the rheological and mechanical viewpoints. The SFRSCC was used to build two series of four slabs of 2550 x 2550 x 150 mm^3 dimensions, tested centrically up to failure in order to assess the effectiveness of steel fibre content and SFRSCC strength class on the behaviour of slabs loaded in punching failure conditions. The experimental program is herein described in detail, and the relevant results are presented and analysed. Furthermore, the effectiveness of fibre reinforcement is assessed by comparing the deformational response, crack patterns and failure modes of the tested slabs. An analytical model is proposed for the prediction of the punching failure load, which is based on the most recent recommendations of *fib* Model Code 2010 [11] for the punching resistance of flat RC slabs and for the characterization of the behaviour of FRC. This model determines two curves, one corresponding to the relationship between the applied load and the rotation of the slab (V-ψ), and the other that represents a failure criterion. The interception of these two curves provides the punching failure load. A simplified and refined formulations were developed, both with excellent predictive capacity in terms of failure load, with a coefficient of variation on the simulations of the tested slabs less than 5.0%. In terms of V-ψ relationship, the more refined approach has predicted with high accuracy the responses recorded experimentally.

2. MATERIALS AND METHODS

2.1. Slab prototypes

The geometry of the slab prototype of the experimental program is represented in Figure 1. The load was applied in the centre of the slab by using a steel plate of 200×200×50 mm^3 placed in between the actuator and the slab.

The flexural reinforcement adopted in the reference slabs and in SFRSCC slabs is represented in Figures 2a and 2b, respectively. In the SFRSCC slabs the reinforcement in the two directions is limited to a strip in the central zone of a width of about $e+6 \cdot d$, where e is the edge of the loading steel plate (200 mm), and d is the internal arm of the slab (Figure 2c). The flexural reinforcement ratio, ρ, in the two main strips was 0.88%, and was equal in all the tested slabs. According to EC2 [12] and CEB-FIP 90 [13], the ρ should be evaluated in a strip of a width of $e+6 \cdot d$, where e is the edge of the cross section of the column (assumed of square configuration). The corresponding equation is $\rho=A_s/A_c=A_s/[(e+6 \cdot d) \cdot d]$, where A_s is the cross sectional area of the flexural reinforcement applied in this strip.

During concrete casting the flexural reinforcement was in the top surface in order to reproduce, as closest as possible, the real conditions when building a flat slab supported on columns. This is an important aspect, since the content of steel fibres tends to increase from the top to the bottom due to the highest mass density of the steel. This effect is more pronounced when fresh concrete is vibrated during casting [10, 14], leading, in general, to larger positive (tensile strains in the bottom surface) than negative resisting bending moments.

The concrete was prepared in a ready mix plant, and two different strength classes were order for an average compressive strength (f_{cm}) of 50 and 70 MPa at 28 days. Each series was designed in order to be composed of a slab without fibre reinforcement and a slab with 60, 75 and 90 kg/m^3 of hooked ends steel fibres of 37 mm length (l_f), 0.55 mm diameter (d_f), 67 of aspect ratio (l_f/d_f), and tensile strength of about 1100 MPa. The full program is described in Table 1. The acronym C_fXf_cY was used to designate the type of slab, where X is the content of steel fibres in kg/m^3, and Y is the average concrete compressive strength. For instance, C_f75f_c50 is the slab that was planned to be of a concrete of f_{cm}=50 MPa, reinforced with 75 kg/m^3 of fibres.

After the punching tests have been executed, the internal arm of the flexural reinforcement, d, was measured in several cross sections, and the average value of d for each slab is indicated in Table 1. Difficulties were faced in assuring a constant d in the slabs of the experimental program, having d ranged between 117 and 133 mm. The ρ indicated in this table was determined by considering the d value measured experimentally.

2.2. Test setup

Figure 3 shows the test setup developed for the execution of the punching tests of the experimental program. The load was applied upward by using an actuator of 1000 kN capacity with a load cell of the same capacity and accuracy of 1 kN. In between the actuator and the bottom surface of the slab, in the central part of the slab, a steel plate of dimensions represented in Figure 2 was used to distribute, as uniformly as possible, the load applied by the actuator. In between the piston of the actuator and the steel plate, a metallic hinge was introduced to minimize the application of parasitic bending moments, and to assure, as much as possible, double symmetry conditions for the test. The test was executed under displacement control, at a displacement rate of 0.05 mm/min in the centre point of the slab.

A slab was supported on twelve dywidag steel bars of 35 mm diameter. Each of these bars has passed through a hole of an average diameter of 60 mm executed after the concrete of the slab has been cured (Figure 3b). The inferior extremity of eight of these bars were simply supported on the reaction floor, while the superior extremity was fixed on the top surface of the slab by using steel plates of 200×200×50 mm^3. Due to restrictions on the pattern of the holes of the reaction slab, steel profiles were used to support four of these dywidag steel bars. Steel tubes were also used to temporarily support the slab when installing the monitoring system.

2.3. Monitoring system

For measuring the deflection of the slab, seven Linear Variable Differential Transducer (LVDT) devices were applied in the points indicated in Figure 4a. The LVDTs were supported in an auxiliary supporting system completely separated from the slab in order to assure that these devices measure only deflections of the slab. Electrical strain gauges (SGs) of 2 mm gauge length and 120 Ω of gauge resistance were applied in the dywidag steel bars to measure the deformability of these bars. To measure the strains in the flexural reinforcement, ten SGs (of characteristics equal to the previous ones) were installed in two steel bars per slab in the positions indicated in Figure 4b (five SGs per each of the two main directions of the flexural reinforcement). Finally, to evaluate the concrete compressive strains in the slab's bottom surface, in the zone where maximum strains were expectable, four SGs were installed in the positions indicated in Figure 4c. These SGs had 30 mm gauge length and 120 Ω of gauge resistance.

2.4. Materials and properties

2.4.1. Concrete

The mix compositions of the eight slabs of the experimental program are indicated in Table 2. Even for the same strength class, the compositions for different content of fibres have some differences in order to take into account the interference of the fibres in the skeleton arrangement of the aggregates, by providing the best arrangement of the concrete constituents and assuring self-compactability requisites without occurrence of segregation for the constituents in all the mixes. By executing slump cone and Lbox tests it was obtained an average value of 615 mm for the spread diameter, and 0.9 for the H_2/H_1 blocking ratio parameter [15].

For each slab, nine cylinders of 150 mm diameter and 300 mm height, nine beams of 150×150×600 mm^3 dimensions, and three round panels of 800 mm diameter and 80 mm thickness were cast and cured in the same conditions of the corresponding slab. The cylinder specimens were used to evaluate the average compressive strength, f_{cm}, and the stress-strain response of concrete in compression [16]. The prismatic specimens were used to determine the flexural tensile strength of the developed concretes, and to evaluate the post-cracking residual flexural tensile strength parameters ($f_{R,i}$) of SFRSCC according to the recommendations of the *fib* Model Code 2010 [11]. The $f_{R,i}$ can be used to define the constitutive law of the SFRSCC for design purposes, by using the recommendations of the *fib* Model Code 2010 [11]. From each three point notched beam-bending test (3PBT) it was obtained a relationship between the applied force and the crack mouth opening displacement (CMOD). By evaluating the force at CMOD of 0.5, 1.5, 2.5 and 3.5 mm, the $f_{R,i}$ are determined by applying the following equation:

$$f_{R,i} = \frac{3 \cdot F_i \cdot L}{2 \cdot b \cdot h_{sp}^{\ 2}} \tag{1}$$

where b (=150 mm) and L (=500 mm) are the width and the span of the specimen, and h_{sp} is the distance between the tip of the notch and the top of the cross section. In an attempt of assuring an unique crack progressing along the notched plane in the three point SFRSCC beam bending tests, the depth of the notch was increased with the content of fibres (25, 42.5 and 60 mm for the C_f=60, 75 and 90 kg/m^3, respectively), as indicated in the second column of Table 4. Therefore, the h_{sp} for the specimens of the series C_f=60, 75 and 90 kg/m^3 was 125, 107.5 and 90 mm, respectively. The flexural stress versus CMOD curves obtained in the 3PBT are presented in Figure 5.

By using the $f_{R,i}$ values, the *fib* Model Code 2010 proposes the following post-cracking residual strength parameter:

$$f_{Ftu} = f_{Fts} - \frac{w_u}{2.5} \cdot \left(f_{Fts} - 0.5 \cdot f_{R3} + 0.2 \cdot f_{R1} \right) \geq 0 ; \qquad f_{Fts} = 0.45 \cdot f_{R1} \tag{2}$$

which is obtained for an ultimate crack opening of w_u=1.5 mm, and later will be used to define the post-cracking constitutive law of the SFRSCC. The obtained values for the f_{Ftu} are indicated in Table 3.

Finally, the round panels were tested according to the ASTM recommendations [17] in order to determine the force *vs.* deflection and the energy absorption *vs.* deflection relationships. The first relationship provides data that can be used in the design of SFRSCC slabs according to the yield line method [18], and the second one indicates the toughness performance of the SFRSCC. The force-deflection and the energy-deflection curves recorded in the round panel tests are depicted in Figure 6.

Table 3 presents the age at which the tests were executed, the f_{cm} and the strain at compressive strength (ε_{cp},) recorded in the compressive tests according to the ISO 1920-3 [16], the limit of proportionality ($f_{fct,L}$) and the $f_{R,i}$ according to *fib* Model Code 2010 [11], the average peak load ($F_{RPT,max}$), and the energy absorption up to 40 mm of deflection ($U_{RPT,40}$) recorded in the round panel tests executed according to the ATSM C-1550 [17]. The coefficient of variation of the obtained results is indicated within round brackets.

Before commenting the results just presented, it should be mentioned that all the concrete mixing and casting procedures of the slabs and corresponding specimens were executed in a ready mix concrete company. The fibres were transported in a treadmill towards the mixer. During the casting process of C_f60f_c50 and C_f75f_c50 slabs it was verified that some fibres inadvertently fell from the treadmill during its transportation to the mixer. Therefore, to estimate the content of fibres (C_f) in the slabs, the number of fibres in the fracture surface (N_f) of the corresponding 3PBT specimens was evaluated according to the strategy described in Barros and Antunes [10]. Considering N_f, and following the approach proposed by Abrishambaf *et al.* [19], the obtained C_f for the tested slabs are presented in Table 4. It is verified that the content of fibres applied in the C_f60f_c50 and C_f75f_c50 compositions seems to have been much lower than the target value, while in the C_f75f_c70 composition the applied content of fibres seems to have been higher than the target value. This had a significant impact on the test results with notched beams, round panels and punching slabs, in a consistent manner, as it will be later demonstrated.

In section 4 more information in respect to the content of fibres actually applied in the tested slabs will be provided, since after the slabs have been tested, cylindrical samples were extracted in order to estimate the fibre distribution along the depth of the slabs. The results confirmed that slabs C_f60f_c50 and C_f75f_c50 had a content of fibres of about 30 Kg/m^3.

The average value of the f_{cm} of the series with a target f_{cm}=50 MPa was 55.4 MPa (with a CoV of about 5%), a little bit higher than the aimed value, while for the series with a target f_{cm}=70 MPa the average value of f_{cm} was 63.5 MPa with a much higher CoV (about 19%). Therefore the difference of the f_{cm} between the two series was about 8 MPa, much lower than the target one (20 MPa), which may have decreased the effect of the concrete strength class on the punching resistance. Unfortunately, the authors of the present paper had not the possibility of controlling the mixing procedures, since due to the relatively large size of the slabs, the SFRSCC was order to a ready concrete company.

The number of fibres in the notched fracture surface of the tested specimens, the corresponding theoretical content of fibres (Table 4), as well as the content of fibres evaluated in the cores extracted from the tested sabs, clearly support the tendency obtained in the results in the notched beam bending tests and in round panel tests presented in Table 3. In fact the $f_{R,i}$ and the $U_{RPT,40}$ have followed closely the obtained C_f.

2.4.2. Steel bars

Five steel bar specimens representative of the conventional flexural reinforcement were submitted to uniaxial tensile tests according to the recommendations of ISO 15630-1 [20]. The average values of the obtained results are indicated in Table 5, where ε_{sy} and f_{sy} are the strain at yield initiation and the corresponding stress, respectively, ε_{su} is the strain at maximum tensile stress, f_{su}, and E_s is the elasticity modulus.

3. EXPERIMENTAL RESULTS

3.1. Force-deflection response

Figure 7 represents the force-deflection relationship in the centre of the tested slabs. Table 6 includes the relevant obtained results, where P_{max} is the maximum applied load, and δ_{Pmax} is its corresponding deflection, P_{max}^{SFRC} and P_{max}^{REF} are the maximum load of a SFRC slab and of its corresponding reference slab, respectively, δ_{max}^{SFRC} and δ_{max}^{REF} are the deflection at P_{max} of a SFRC slab and of its corresponding reference slab, respectively. This table also includes the failure mode observed in each slab. Despite the large dispersion of results, mainly in series of f_{cm}=70 MPa, Figure 8 shows a clear tendency of an increase of the load carrying capacity of the slabs with the increase of $f_{R,i}$ and $U_{RPT,40}$. This dispersion is justified by the large variation of the average compressive strength in this series, which provided different levels of fibre reinforcement effectiveness.

Nonetheless, these results evidence that the properties at the material level, such as the case of the number of fibres in the fracture surface of the notched beam bending tests, the post-cracking residual strength parameters, and the energy absorption determined in the round panel tests, seem to be good indicators of slab's load carrying capacity. In fact, a tendency for a linear relation between P_{max} and these parameters is observed.

Due to the relative low content of fibres in the C_f60f_c50 and C_f75f_c50 slabs (around 30 Kg/m^3), they have failed in punching like the corresponding reference slabs (see Table 6). This can be also justified by the relatively low values obtained for f_{Ftu} for these SFRSCC (Table 3). In fact, Figure 8f shows that an almost linear tendency is observed between f_{Ftu} and P_{max}.

The results in Table 6 show that in series f_{cm}=50 MPa the increase in terms of maximum load was only significant (12%) in the *Cf90fc50* that has failed in bending, while in series f_{cm}=70 MPa this increase has attained 24% in the C_f75f_c70 and C_f90f_c70 slabs. Table 1 shows that the internal arm (d) of the flexural reinforcement of the C_f90f_c50 and C_f90f_c70 slabs was smaller than the d of the corresponding reference slabs (7 to 10%). Therefore, if in the SFRC slabs a d value equal to the corresponding reference slabs had been assured, a higher increase of $P_{max}^{SFRC} / P_{max}^{REF}$ would have been obtained. The influence of the concrete compressive strength in the punching failure load can be assessed by analysing C_f75f_c70 and C_f90f_c70 slabs. In fact, Table 3 shows that these slabs were built with concrete of relatively different average compressive strength (70.02 and 57.63 MPa, respectively), but these concretes were, in reality, reinforced with similar content of fibres (86 and 79 Kg/m^3, respectively, see Table 4). This means that these SFRSCC have similar post-cracking residual strength (Table 3), resulting an almost equal load carrying capacity for these slabs. This evidences the relevance of the post-cracking residual strength of the SFRSCC on the slab's load carrying capacity. In case of C_f90f_c50 (f_{cm}=56.39 MPa) and C_f75f_c70 (f_{cm}=70.02 MPa) slabs that have different strength class, but similar content of fibres and identical f_{Ftu} (Table 3), the later slab presented a P_{max} 10% higher, which indicates that the f_{cm} has also a relevant impact on the load carrying capacity of this type of slabs. However, if the internal arm of the flexural reinforcement of these slabs is considered in this analysis, it can be concluded that the post-cracking residual strength of the SFRC seems to have higher influence in the slab's load carrying capacity than the concrete average compressive strength. In fact, Table 1 shows that the internal arm of the flexural reinforcement of the C_f90f_c50 and C_f75f_c70 slabs was 118 and 128 mm, respectively, which suggests that if equal internal arm had been assured, the difference on the P_{max} for these slabs would have been smaller.

In terms of deflection at maximum load, $\delta_{P\,max}$, the increase of the $\delta_{max}^{SFRC} / \delta_{max}^{REF}$ ratio, as expected, was only significant in the slabs failing in bending (Table 6). This increase has ranged from 54% to 102% in the series f_{cm}=70 MPa (it has increased with C_f), and it was 72% in C_f90f_c50 slab. The relatively low content of fibres really introduced in the C_f60f_c50 and C_f75f_c50 slabs (about 30 Kg/m^3) has only contributed for a small increase of the deflection at punching failure load (4 to 6%).

3.2. Strains in concrete

The variation of concrete strains recorded in the SG_C1 strain gauges (Figure 4c) during the loading process is represented in Figure 9 for the slabs of both series. The strain variation presented a similar trend, with a continuous increase of strain up to a load level close to the maximum load, and then a gradual decrease has occurred with an inversion from compressive to tensile strain in almost all the slabs. A tendency for an increase of the maximum compressive strains ($\varepsilon_{c1,max}$) with the increase of the load carrying capacity is observed (Table 7), as expected, but $\varepsilon_{c1,max}$ was well smaller than the strain at compressive strength ($\varepsilon_{cp,exp}$), Table 3. In Table 7 the positive strain values represent compressive strains. In this table $\varepsilon_{c1,Pmax}$ is the strain at P_{max}, $P_{\varepsilon c1,max}$ is the load when $\varepsilon_{c1,max}$ was registered, $\varepsilon_{c1,min}$ and $P_{\varepsilon c1,min}$ are the minimum strain and the load when it was recorded, respectively, and $\delta_{\varepsilon c1,\max(\min)} / \delta_{P\max}$ is the ratio between the deflection when $\varepsilon_{c1,max(min)}$ was registered and the deflection at P_{max}, whose values are indicated in Table 6. According to Muttoni [21], the occurrence of radial tensile strains in the concrete compressed surface close to the column is an indicator of punching failure; however, radial tensile strains were also registered in the tested slabs that failed in bending.

3.3. Strains in steel bars

Due to a deficient functioning of several strain gauges installed in the steel bars, mainly in the SFRSCC slabs, the information expected to extract from these sensors was too scarce for deriving relevant conclusions. Nonetheless, based on the registered information, it was possible to evaluate the value of r_y, which is the distance from the slab's centre that defines the region where the rebars have yielded ($\varepsilon_s \geq \varepsilon_{sy}$) at the failure of the slab (Figure 10). In this figure r_s is the radius of the slab. The r_y parameter was determined by intercepting the diagram of the variation of strains, in the alignment where the strain gauges were installed, with the line corresponding to the yield strain of the steel bars (ε_{sy}=2.53‰). The obtained values are indicated in Table 8, where data from other experimental programs are also included. In this table the "Load level" represents the load at which r_y was measured. The results obtained in the SFRC slabs indicate that the value of r_y at failure of the slab has varied between $0.30 \cdot r_s$ and $0.45 \cdot r_s$. Based on the analysed data, an average value of 0.37 was obtained for the r_y/r_s ratio, which confirms the value of 0.35 adopted by Moraes-Neto *et al.* [22].

3.4. Crack patterns and failure modes

The crack patterns registered at the end of the tests of the slabs of the experimental program are shown in Figure 11. It is verified that fibres have provided a more diffuse crack patterns due to the arrestment of crack propagation provided by reinforcement mechanisms of fibres bridging the cracks.

In the C_f0f_c50 and C_f0f_c70 reference slabs (Figure 11a and 11b), radial cracks started being visible at a load level of about $0.30 \cdot P_{max}$, and have propagated in the loaded area and its vicinity up to $0.80 \cdot P_{max}$. At this load level, circumferential cracks started being visible and have propagated up to the attainment of the punching failure load, while the number of radial cracks has stabilized, but the crack width has increased up to the failure of the slabs. Table 9 indicates the load level when the first radial crack and the first circumferential crack were visible in the tested slabs. Figure 12, which shows the cross section coinciding with the section A-A represented in Figure 2a and 2b, evidences the geometry of the punching failure surface formed in the tested slabs (the section was cut 50 mm far from the symmetry axis of the slab in order to avoid cutting steel bars). The data defining the geometry of the punching failure surface is included in Table 10, by using the symbols adopted in Figure 13. The $r_{0,avg}$ is the average value of r_0, while θ_{avg} is the average value of the inclination of the punching failure crack. The C_f60f_c50 and C_f60f_c70 slabs had similar fracture process up to a load level of about $0.85 \cdot P_{max}$ (Figure 11c and 11d). The first cracks were detected in the interval $0.3\text{-}0.4 \cdot P_{max}$, close to the loaded area, followed by the propagation of radial cracks up to $\approx 0.85 \cdot P_{max}$. At this load level circumferential cracks started being visible. In C_f60f_c50 slab this type of cracks has progressed around the loaded area in the subsequent loading stages up to the occurrence of punching failure (Figure 12c), while in C_f60f_c70 slab the circumferential cracks did not propagate, and flexural cracks became dominant along the main axis of the slab (Figure 11d) leading to the flexural failure of this slab. This is justified, mainly, by the quite different content of fibres really applied in these slabs, about 30 and 53 Kg/m^3 in C_f60f_c50 and C_f60f_c70 slabs, respectively (Table 4). In fact, Figure 12c shows that the relatively low content of fibres applied in C_f60f_c50 slab was not enough to avoid the formation of the punching failure cone (but with failure cracks with higher inclination than failure cracks of the reference slabs). However, in the C_f60f_c70 slab the larger content of fibres has promoted the occurrence of several cracks, of shear and flexure nature, but the propagation of flexural failure cracks have prevailed. The higher concrete compressive strength of the C_f60f_c70 slab has also contributed for this different response of these slabs at ultimate limit stages.

In the C_f75f_c50 and C_f75f_c70 slabs the cracking propagation process was similar up to the load level $\approx 0.80 \cdot P_{max}$. (Figure 11e and 11f). The first cracks have formed around the loaded area at a load level $\approx 0.30 \cdot P_{max}$, and propagated radially up to a load level of $\approx 0.80 \cdot P_{max}$ has been attained. Above this load level the damage due to crack propagation in the C_f75f_c50 slab has conducted to the formation of punching failure mode, with the geometry of the failure surface shown in Figure 12e. The relatively reduced content of fibres really applied in this slab (32 Kg/m^3, see Table 4) justifies the incapacity to avoid the occurrence of the punching failure in this slab. In the case of the C_f75f_c70 slab, the content of fibres was enough to assure a flexural failure mode, with the formation of four main flexural failure cracks at ultimate stage (Figure 11f). Figure 12f shows the formation of several cracks of flexural and shear nature, but the flexural ones have prevailed at failure stage. The best structural performance of this slab (Table 6) is justified by the highest content of fibres (Table 4) and the highest compressive strength (Table 3).

The cracking propagation process of C_f90f_c50 and C_f90f_c70 was similar up a load level $\approx 0.75 \cdot P_{max}$ (Figure 11g and 11h). The first cracks have formed around the loaded area at a load level $\approx 0.25 \cdot P_{max}$, and propagated radially up to a load level $\approx 0.75 \cdot P_{max}$ has been attained. At this load level the first circumferential cracks were detected, and at $\approx 0.90 \cdot P_{max}$ the localization of flexural failure cracks along the main axis of the slab started occurring. Figure 12h shows that a punching failure surface has occurred in the C_f90f_c70 slab, but this occurrence was observed for a very high deflection of this slab, at about 53mm. In the C_f90f_c50 slab a punching failure cone was not formed (Figure 12g), and four dominant flexural failure cracks were localized along the main axes of the slab (Figure 11g).

4. THEORETICAL MODELS AND ANALYSIS

4.1. Model formulation

The model that is herein proposed determines the punching resistance of a SFRC flat slab by defining two curves, one corresponding to the relationship between the applied load and the rotation of the slab (V-ψ), and the other that represents a failure criterion. The interception of these curves provides the punching failure load. The V-ψ relationship is based on the recommendations of Muttoni [21] and on the most recent concepts proposed by *fib* Model Code 2010 [11] for the characterization of fibre reinforced concrete. For the establishment of the V-ψ relationship, the column-slab connection is assumed in axisymmetric conditions (Figure 14a). The crack pattern of a slab failing in punching can be assumed as forming radial segments (Figures 14a and 14b). Each radial segment is delimited by a tangential crack formed close to the column, by two radial cracks, and by the edge considered as a free boarder of the slab (Figure 14b).

4.1.1. Load-rotation approach

According to Guandalini [26] the V-ψ relationship of an axisymmetric slab can be obtained by using the 2L bilinear moment-curvature diagram (m-χ) represented in Figure 14c.

To derive the load versus rotation relationship supported on the 2L m-χ diagram, it is necessary to assume the slab decomposed in two regions: elastic ($r_y<r_0$) and elasto-plastic ($r_0<r_y<r_s$). By executing equilibrium of bending moments of the force components installed in the radial segment represented in Figure 14b, it is obtained the following two equation after some mathematical manipulations described elsewhere [22]:

$$V(\psi) = \frac{2 \cdot \pi}{(r_q - r_c)} \cdot E \cdot I_1 \cdot \psi \cdot \left[1 + ln\left(\frac{r_s}{r_0}\right)\right] \qquad \textit{for } r_y \le r_0 \textit{ (elastic regime)} \tag{3a}$$

$$V(\psi)=\frac{2\cdot\pi}{(r_q-r_c)}\cdot E\cdot I_1\cdot\psi\cdot\left[1+ln\left(\frac{r_s}{r_y}\right)\right] \qquad \textit{for } r_0<r_y<r_s \textit{ (elasto-plastic regime)} \tag{3b}$$

In these equations the variables r_c, r_0, r_q and r_s represent, respectively, the radius of column's cross section, the distance to the axis of the column to the punching failure surface ($r_0=r_c+d/2$), the distance of the circumferential loading line, and the radius of the slab. The $E{\cdot}I_1$ represents the flexural stiffness of the slab's cross section after crack initiation (Figure 14c).

The evaluation of $E{\cdot}I_1$, was executed following the procedures adopted for RC members [18], and assuming a stabilized cracking phase:

$$E\cdot I_1=\rho\cdot\beta\cdot E_s\cdot d^3\cdot\left(1-\frac{x}{d}\right)\cdot\left(1-\frac{x}{3\cdot d}\right) \tag{4}$$

The contribution of fibre reinforcement for the $E{\cdot}I_1$ is only indirectly taken in the evaluation of the neutral axis, x, Figure 15 (η and λ parameters are evaluated according to [11], and f_{Ftu} according to equation (2)). In Eq. (4) β is a factor intending to take into account the arrangement of the reinforcement, since the deduction of Eqs. (3) was supported on the principle of axisymmetric structural conditions, but the majority of the built and tested RC flat slabs have orthogonal arrangement of the reinforcement [26]. According to Muttoni [21], β=0.6 yields satisfactory results. The evaluation of the position of the neutral axis, x, was made according to the recommendations of *fib* Model Code 2010 [11], see Figure 15.

To evaluate f_{Ftu} according to equation (2), the values of f_{R1} and f_{R3} obtained experimentally can be used, or, alternatively, as demonstrated in [28], the following equations can also be adopted that are determined based on statistical analysis of a database that collects results from 3PBT in SFRC:

$$f_{R1}=7.5\cdot\left(C_f\cdot\frac{l_f}{d_f}\right)^{0.8}; \qquad f_{R3}=6.0\cdot\left(C_f\cdot\frac{l_f}{d_f}\right)^{0.7} \qquad \text{[MPa]} \tag{5}$$

In Figure 16 is represented the relationship between ψ and (V/V_{flex}) obtained from the tested slabs, where V_{flex} is the load corresponding to the flexural failure of the slab that can be determined from the following equation [22].

$$V_{flex}=2\cdot\pi\cdot m_R\cdot\frac{r_s}{(r_q-r_c)} \qquad \textit{for } r_y=r_s \textit{ (flexural failure load)} \tag{6}$$

where m_R represents the resisting bending moment (plastic bending moment) of the slab's cross section. The solid and dashed lines in Figure 16 represent, respectively, the experimental results and the curves that best fit the experimental results. The results in this figure evidence that the slab's rotation is proportional to $(V/V_{flex})^2$. For a more reliable ψ-(V/V_{flex}) relationship, the results obtained from the experimental works carried bout by Nguyen-Minh *et al.* [9], Cheng and Parra [25], Azevedo [24] and Holanda [27] were also considered, leading to a direct proportionality between ψ and $\left(V/V_{flex}\right)^{3/2}$:

$$\psi \alpha \left(V/V_{flex}\right)^{3/2} \tag{7}$$

Combining equations (3) and (6) and assuming for the r_y/r_s the value of 0.35 obtained in Section 3.3, and after executing some mathematical manipulations, described in [22], the following equation was obtained:

$$\psi = \Delta \cdot \frac{m_R \cdot r_s}{E \cdot I_1} \cdot \left(\frac{V}{V_{flex}}\right)^{3/2} \tag{8}$$

where Δ=0.65 for regular concrete and Δ=1.625 for concrete of lightweight aggregates. For slabs in axisymmetric structural conditions, V_{flex} is obtained from Eq. (6), while for square slabs the yield line theory leads $V_{flex}=8 \cdot m_R$.
To evaluate the plastic bending moment, m_R, the recommendations of *fib* Model Code 2010 [11] for the simulation of the contribution of fibre reinforcement are adopted in the present work (see Eq. (2) and Figure 15).

4.1.2. Failure criterion

Following the recommendations of ACI 318 [33], Muttoni [21], and Muttoni and Schwartz [29], and taking the main achievements of Walraven [30], and Vecchio and Collins [31] on the contribution of the aggregate interlock for the concrete shear resistance, and the relevant results of Moraes-Neto [28] on the contribution of fibre reinforcement for the concrete shear resistance, the following equation was determined that defines the punching failure criterion of *SFRC* slabs:

$$\frac{V}{b_0 \cdot d \cdot \sqrt{f_c} \cdot \left[\lambda_f + k_f^{\,1/3}\right]} = \frac{1}{1.33 + 20 \cdot \mu_f \cdot \psi \cdot d \cdot k_{dg}} \quad \text{[MPa, mm]} \tag{9}$$

where b_0 is the perimeter of the punching failure surface ($b_0 = 4 \cdot e + \pi \cdot d$ for column of square cross section), k_{dg}=1/(d_{g0}+d_g), being d_{g0}=16 mm the reference diameter, and d_g the maximum diameter of the aggregates, and:

$$k_f = C_f \cdot \frac{l_f}{d_f}; \qquad \lambda_f = \begin{cases} 0\, if\ C_f \neq 0 \\ 1\, if\ C_f = 0 \end{cases}; \qquad \mu_f = \begin{cases} (1/11)\ if\ C_f \neq 0 \\ 1\ if\ C_f = 0 \end{cases} \tag{10}$$

4.2. Predictive performance of the model

4.2.1. Simplified approach on the evaluation of the resisting bending moment, $\boldsymbol{m_R}$

In the present approach, the resisting bending moment, m_R, is calculated by applying the stress distribution diagram represented in Figure 15, the $E{\cdot}I_1$ is calculated from equation (4), and for the evaluation of equation (9) and f_{Ftu} the values of the content of fibres, C_f, included in the last column of Table 4 were adopted. By adopting this approach, the results presented in Table 11 in the columns corresponding to "Simplified" were obtained. In this table, P_{max}^{exp} and $P_{\max}^{the}$ is the maximum load obtained experimentally and applying the theoretical formulation, respectively. The V-ψ relationships of the tested slabs, recorded experimentally and determined with the theoretical formulation, are compared in Figure 17. The results included in Table 11 shows that the simplified theoretical model provides predictions slightly against safety, since the average value of $P_{max}^{exp} / P_{max}^{the}$ is 0.88, but the CoV is relatively small (4.4%). The curves in Figure 17 evidence that the simplified theoretical model predicts a less stiff V-ψ response and higher ultimate load than the corresponding experimental results. This is caused by the simplified methodology on the evaluation of the slab's flexural stiffness, $E{\cdot}I_1$, as well as on the determination of the resisting bending moment of the slab's cross section m_R.

4.2.2. Refined approach on the evaluation of the resisting bending moment, $\boldsymbol{m_R}$

To overcome the deficiencies of the simplified theoretical model, the following procedures were adopted: i) determine the distribution of fibre content along the depth of the slab, since it is well recognized that the content of fibres has a tendency to increase from the top to the bottom of the structural elements in consequence of the highest mass density of the steel [10]; ii) use a cross section layer model that is capable of determining the m-χ diagram of the slab's cross section by using different constitutive laws for each layer, such is the case of the *software* DOCROS (***D****esign* ***Of*** ***CRO****ss*-***S****ections*) [32].

To perform the procedure i), after the slabs have been tested three cylinder specimens per slab were extracted from the positions indicated in Table 12 (the coordinates are related to the centre of the slab). These cylinders had a diameter of 100mm and a height equal to the thickness of the corresponding slab. Each cylinder specimen was cut in three slices of equal thickness, and the designation of "Top", "Intermediate" and "Bottom" was attributed accordingly. In columns 6, 7, and 8 to 10 of Table 12 are presented the average content of fibres (in Kg/m^3) on the cylinder, on the slab, and on each slice, respectively. The obtained results have confirmed that about 30 Kg/m^3 of fibres were applied in the slabs C_f60f_c50 and C_f75f_c50. Furthermore, it is verified a tendency of the fibre content to increase from the top to the bottom of the slab, with $C_{f,avg,bottom} \approx 1.5 \cdot C_{f,avg,top}$, which justifies the obtained overestimation of the m_R when the simplified approach was used.

To attend the aforementioned procedure ii), a cross section layer model available in the DOCROS computer program was used [32]. This model assumes that a plane section remains plane after deformation, and bond between materials is perfect. The section is divided in horizontal layers, and the thickness and width of each layer is user-defined and depend on the cross-section geometry.

For the present study, the slab's cross section was decomposed on the layered configuration schematically represented in Figure 18. The cross section was formed by 15 layers, $h=12 \cdot t_{c,1}+t_s+2 \cdot t_{c,2}$=150 mm. The symbols corresponding to $t_{c,1}$, $t_{c,2}$ and b_c=1000 mm are attributed to SFRSCC layers, while t_s=10 mm and b_s define the cross section area of the flexural reinforcement ($t_s \cdot b_s=A_s=\rho \cdot d \cdot b_c$). The values of $t_{c,1}$ and $t_{c,2}$ were determined in order to obtain the d values indicated in Table 1.

By considering the average C_f values obtained for each slice, and adopting Eq. (8) for determining f_{R1} and f_{R3}, the post-cracking stress-strain constitutive law of the layers representative of a slice was determined according to the recommendations of *fib* Model Code 2010 [11]. For modelling the compression behaviour of the SFRSCC and the tension-compression behaviour of the flexural reinforcement, the stress-strain relationship of the corresponding models available in DOCROS was adopted, by considering the data indicated in Table 3 and Table 5, respectively. The obtained constitutive laws for the SFRSCC are represented in Figure 19, while the determined moment-curvature relationships are indicated in Figure 20.

By adopting this approach, the results presented in Table 11 in the columns corresponding to "Refined" were obtained. The V-ψ relationships of the tested slabs, recorded experimentally and determined with the theoretical formulation, are compared in Figure 17. The results included in Table 11 shows that the refined theoretical model predicts with excellent accuracy ($P_{max}^{exp}/P_{max}^{the}$=0.95) and small CoV (4.83%) the results obtained experimentally. The curves in Figure 17 evidence that the refined theoretical model predicts with high accuracy the full V-ψ response recorded experimentally.

By considering the m_R and $E \cdot I_1$ obtained with the simplified and refined models, it was verified that the simplified approach can provide results of an accuracy similar to the ones obtained with the refined model if the m_R and $E \cdot I_1$ are adjusted according to the following proposal: $m_{R,adjusted} \approx 0.90 \cdot m_{R,simple}$; $(E \cdot I)_{adjusted} \approx 1.41 \cdot (E \cdot I)_{simple}$.

5. CONCLUSIONS

In this paper an experimental program was carried out to assess the influence of steel fibre reinforcement for the punching resistance of flat slabs centrically loaded.

Based on the results obtained in experimental and analytical work, the following observations can be pointed out:

- A clear linear relationship was observed between the residual flexural tensile strength parameters, $f_{R,i}$, of steel fibre reinforced self-compacting concrete (SFRSCC) obtained from the three point notched beams bending tests and the load carrying capacity of the tested slabs, P_{max}. A linear relationship was also observed between the energy absorption capacity, $U_{RPT,40}$, of SFRSCC assessed by round panel tests and P_{max}. This indicates that the performance of the SFRSCC slabs can be estimated by using this type of tests that are adopted for the material characterization and quality control;
- Based on the results from the punching tests, a concrete of f_{cm} between 50 and 70 MPa reinforced with a volume of about 1% of hooked ends steel fibres can assure a flexural failure mode and a very ductile behaviour, as long as a fibre type is selected that avoid fibre rupture;
- In this type of SFRSCC the average values of $f_{R,1}$ and $f_{R,3}$ have varied between 11-13 MPa and 12-13 MPa, respectively, representing these values the flexural resistance for a crack width of 0.5 mm and 2.5 mm. This type of SFRSCC has provided an increase in terms of load carrying capacity ranging between 12 and 24%, depending on the f_{cm}, with the tendency of increasing with the $f_{R,i}$ and f_{cm}, as expected;
- In terms of maximum deflection at failure, the increase provided by this type of SFRSCC has varied between 72% and 102%, with also the tendency of increasing with the $f_{R,i}$ and f_{cm}.
- An analytical model was developed for the prediction of the punching resistance of SFRC flat slabs. This model determines two curves, one corresponding to the relationship between the applied load and the rotation of the slab (V-ψ), and the other that represents a failure criterion. The interception of these curves provides the punching failure load. The most refined version of this model was capable of predicting the punching resistance of the tested slabs with excellent accuracy and coefficient of variation of about 5%.

6. ACKNOWLEDGEMENTS

The study presented in this paper is a part of the research project titled "*SlabSys-HFRC - Flat slabs for multi-storey buildings using hybrid reinforced self-compacting concrete: an innovative structural system*", with reference number of PTDC/ECM/120394/2010. The second author acknowledges the support provided by the CAPES and CNPq grant, and the grant provided by the project *SlabSys*. The Authors would acknowledge the collaboration of Casais Company on the preparation of the moulds and flexural reinforcement, CiviTest on the design of the

SFRSCC for the slabs, and Maccaferri, Secil (Unibetão), and Sika companies for the supplying of steel fibres, concrete and superplasticizers, respectively.

7. REFERENCES

[1] PCA – Portland Cement Association. Economical Concrete Floor System, 2005.

[2] Delahay, P.E.J.; Christopher, P.E.B. Current trends in economical concrete construction, Part one: Floor framing and lateral systems. Structure Magazine, pp. 19-21, July, 2007.

[3] Gardner, N.J.; Huh, J.; Chung, L. Lessons from the Sampoong department store collapse. Cement & Concrete Composites, 24, pp. 523-529, 2002.

[4] Maghsoudi, A.A.; Sharifi, Y. Ductility of high strength concrete heavily steel reinforced members. Scientia Iranica, v. 16, nº 4, pp. 297-307, August, 2009.

[5] Melo, G.S.; Coelho, A.E.G.; Oliveira, D.R.C. Reinforced concrete flat slabs with inclined stirrups as shear reinforcement. International Workshop on Punching Shear Capacity of RC Slabs – Proceedings. TRITA-BKN, Bulletin 57, pp. 155-162, 2000.

[6] Choi, H.K.; Beck, S.W.; Baik, Y.S.; Choi, C.S. A study on shear reinforcement of exterior joints for flat plate. Key Engineering Materials, v. 385-387, pp. 865-868, July, 2008.

[7] Tan, K-H.; Paramasivam, P. Punching shear strength of steel fiber reinforced concrete slabs. Journal of Materials in Civil Engineering, v. 6, nº 2, pp. 240-253, May, 1994.

[8] Prisco, M.; Felicetti, R. Some results on punching shear in plain and fibre-reinforced micro-concrete slabs. Magazine of Concrete Research, v. 49, no 180, pp. 201-219, September, 1997.

[9] Nguyen-Minh, L.; Rovňák M.; Tran-Quoc T.; Nguyen-Kim, K. Punching shear resistance of steel fiber reinforced concrete flat slabs. In: Proceedings of the twelfth east Asia–Pacific conference on structural engineering and construction (EASEC-12). Hong Kong Special Administrative Region, China (with CD-rom); 24-26th, pp. 535-6, January, 2011.

[10] Barros, J.A.O.; Antunes, J.A.B.. Experimental characterization of the flexural behaviour of steel fibre reinforced concrete according to RILEM TC 162-TDF recommendations. RILEM TC 162 TDF Workshop, pp. 77-89, March, 2003.

[11] *fib* Model Code 2010 "CEB-FIP Model Code 2010 – Final draft", Thomas Thelford, Lausanne, Switzerland, 2011.

[12] EUROCODE2. Design of Concrete Structures. Part 1-1: General Rules and Rules for Buildings. European Standard, 2004.

[13] CEB-FIP 90. Model Code 1990: Final Draft. Bulletin D'Information, n° 203-205, CEB, Lausanne, July, 1991.

[14] Alves, N.; Barros, J.A.O.; Nunes, Â; Lourenço, L.A.P.. Steel fibre reinforced self-compacting concrete for grid foundations of single-family houses. 8th RILEM International Symposium on Fibre Reinforced Concrete: challenges and opportunities, Eds: Joaquim Barros *et al.*, 12 pp., September, 2012.

[15] EFNARC, Specification and Guidelines for Self-Compacting Concrete (2002), ISBN, 0 9539733 4 4, 32 pp.

[16] ISO 1920-3. Testing of concrete – Part 3: Making and curing test specimens. International Standard, First edition, October, 2004.

[17] ASTM International, Standard C-1550, "Standard Test Method for Flexural Toughness of Fiber Reinforced 305 Concrete (Using Centrally Loaded Panel)", ASTM International, West Conshohocken, 2012.

[18] Barros, J.A.O.; Salehian, H.; Pires, N.M.M.A., Gonçalves, D.M.F.. Design and testing elevated steel fibre reinforced self-compacting concrete slabs. 8th RILEM International Symposium on Fibre Reinforced Concrete: challenges and opportunities, Eds: Joaquim Barros *et al.*, 12 pp., September, 2012. http://hdl.handle.net/1822/21572

[19] Abrishambaf, A.; Barros, J.A.O.; Cunha, V. M. C. F.. State of Art: Fibre Orientation and Dispersion. Technical Report No. 11-DEC/E-30, University of Minho, 22 pp., April, 2011.

[20] ISO 15630-1. Steel for the reinforcement and prestressing of concrete - Test methods -Part 1: Reinforcing bars, wire rod and wire. International Standard, First edition, April, 2002.

[21] Muttoni, A. Punching shear strength of reinforced concrete slabs without transverse reinforcement. ACI Structural Journal, v. 105, nº 4, pp. 440-450, July/August, 2008.

[22] Moraes-Neto, B.N.; Barros, J.A.O.; Melo, G.S.S.A.. A model for the prediction of the punching resistance of steel fibre reinforced concrete slabs centrically loaded. Building Materials Journal, 46, pp. 211-223, 2013.

[23] Mcharg, P. J. Effect of fibre-reinforced concrete on the performance of slab-column specimens. Montreal-Canada. Master thesis. McGill University, 1997.

[24] Azevedo, A.P. Resistance and ductility of slab-column connections on high strength concrete flat slabs with steel fibers and shear reinforcement. Master thesis, School of Engineering of São Carlos, University of São Paulo, EESC-USP, 1999. (in Portuguese)

[25] Cheng, M-Y.; Parra-Montesinos, G.J. Evaluation of steel fiber reinforcement for punching shear resistance in slab-column connections – Part I: Monotonically increased load. ACI Structural Journal, v. 107, nº 1, pp. 101-109, Jan/Feb, 2010.

[26] Guandalini, S. Poinçonnement symétrique des dalles en béton armé. *PhD Thesis* 3380, Ecole Polytechnique Fédérale de Lausanne, Switzerland, 2005. (in French)

[27] Holanda, K.M.A. Analysis of resistant mechanisms and similarities of the adition effect of steel fibers on strength and ductility to both punching shear of flat and the shear of concrete beams. *PhD Thesis*. São Carlos, Brazil, 2002. (in Portuguese)

[28] Moraes-Neto, B.N. Punching behaviour of steel fibre reinforced concrete slabs submitted to symmetric loading. *PhD in Civil Engineering*, Department of Civil and Environmental Engineering, University of Brasília, Brasília, DF, January, 2013. (in Portuguese)

[29] Muttoni, A.; Schwartz, J. Behaviour of Beams and Punching in Slabs without Shear Reinforcement. *IABSE Colloquium*, 62, 703-708, Zurich, Switzerland, 1991.

[30] Walraven, J.C. Fundamental Analysis of Aggregate Interlock. *Journal of Structural Engineering*, ASCE, 107(11), 2245-2270, 1981.

[31] Vecchio, F.J.; Collins, M.P. The Modified Compression-Field Theory for Reinforced Concrete Elements Subjected to Shear. *ACI JOURNAL*, Proceedings 83(2), 219-231, 1986.

[32] Basto, C.A.A.; Barros, J.A.O., "Numeric simulation of sections submitted to bending", Technical report 08-DEC/E-46, Dep. Civil Eng., School Eng. University of Minho, pp. 73, 2008.

[33] ACI 318. Building Code Requirements for Structural Concrete, *American Concrete Institute*, Farmington Hills, Michigan, 2008.

NOTATION

A_c	Cross sectional area of the concrete (in this strip)
A_s	Cross sectional area of the reinforcement (in this strip)
A'_s	Cross sectional area of the compression reinforcement
b	Width of the notched beam
b_0	Critical perimeter for punching shear
C_f	Content of fibre
d	Internal arm of the slab
d_f	Diameter of fibre
d_g, D_{max}	Maximum diameter of the aggregates
d_{g0}	Reference diameter of the aggregates
e	Edge of the loading steel plate
E	Modulus of elasticity of concrete
E_s	Modulus of elasticity of reinforcement
f_{cm}, f_c	Average compressive strength
F_{cr}	Internal compressive force of concrete in radial direction
F_{ct}	Internal compressive force of concrete in tangential direction
$f_{fct,L}$	Limit of proportionality
f_{Fts}	Post-cracking strength for serviceability crack opening
f_{Ftu}	Post-cracking strength for ultimate crack opening
F_i	Load corresponding to CMOD=$CMOD_i$ (notched beam bending test)
$f_{R,i}$	Flexural tensile strength
$F_{RPT,max}$	Average peak load (round panels test)
F_s	Internal force of tensile reinforcement
F'_s	Internal force of compressive reinforcement
F_{sr}	Internal tensile force of reinforcement in radial direction
F_{st}	Internal tensile force of reinforcement in tangential direction
f_{su}	Maximum tensile stress
f_{sy}	Stress at yield initiation
h	Slab thickness
h_{sp}	Distance between the tip of the notch and the top of the cross section beam (notched beam bending test)
H_1, H_2	Lbox tests parameter
I_0	Second moment of area of uncracked concrete cross-section
I_1	Second moment of area of cracked concrete cross-section
l_f	Length of fibre
L	Span of the notched beam
m	Bending moment
m_{cr}	Bending moment at crack initiation
m_R	Resisting bending moment (plastic bending moment)
N_f	Number of fibres in the fracture surface (notched beam bending test)
P_{max}	Maximum load (punching test)
P_{max}^{exp}	Experimental maximum load
P_{max}^{REF}	Reference slab maximum load

P_{max}^{SFRC}	SFRC slab maximum load
P_{max}^{the}	Theoretical maximum load
$P_{\varepsilon c1,max}$	$\varepsilon_{c1,max}$ load
$P_{\varepsilon c1,min}$	$\varepsilon_{c1,min}$ load
r_0	Radius of the critical shear crack
$r_{0,avg}$	Average value of r_0
r_q	Radius of the load introduction at the perimeter
r_s	Radius of circular isolated slab element
r_y	Radius of yielded zone
t_i	Layer of slab’s cross section
$U_{RPT,40}$	Energy absorption up to 40 mm of deflection (round panels test)
V	Shear force
V_{flex}	Shear force associated with flexural capacity of the slab
V_R	Nominal punching shear strength
w_u	Ultimate crack opening
x	Neutral axis of slab
β	Efficiency factor of the bending reinforcement for stiffness calculation
δ_{Pmax}	Deflection at maximum load
δ_{max}^{SFRC}	P_{max}^{SFRC} deflection
δ_{max}^{REF}	P_{max}^{REF} deflection
$\delta_{\varepsilon c1,max}$	$\varepsilon_{c1,max}$ corresponding deflection
$\delta_{\varepsilon c1,min}$	$\varepsilon_{c1,min}$ corresponding deflection
$\Delta\varphi$	Angle of a cracked radial segment of slab
ε_c	Concrete strain
ε_{cu}	Ultimate strain of concrete in compression zone
ε_{fu}	Ultimate strain of fibre in tensile zone
ε_s	Strain of steel reinforcement in tensile zone
ε_{su}	Ultimate strain of steel reinforcement in tensile zone
$\varepsilon_{t,bot}$	Concrete tensile strain at the bottom surface of the slab
$\varepsilon_{c1,max}$	maximum compressive strains (recorded in the SG_C1 strain gauge)
$\varepsilon_{c1,min}$	minimum compressive strains (recorded in the SG_C1 strain gauge)
ε_{cp}	Strain at peak compressive strength
$\varepsilon_{cp,exp}$	Strain at compressive strength
ε_s	Rebar strain
ε_{su}	Strain at maximum tensile stress
ε_{sy}	Strain at yield initiation
θ	Inclination of the punching failure crack
θ_{avg}	Average value of the θ
ρ	Reinforcement ratio
ρ'	Compressive reinforcement ratio
$\sigma_{f,r}$	Post cracking tensile strength of SFRC in radial direction
$\sigma_{f,t}$	Post cracking tensile strength of SFRC in tangential direction
χ_1	Curvature in stabilized cracking
χ_{cr}	Curvature at cracking
χ_y	Yielding curvature
χ	Curvature
ψ	Rotation of slab

LIST OF TABLE CAPTIONS

Table 1. Characteristics of the experimental program.

Table 2. Concrete compositions for the slabs of the experimental program.

Table 3. Average values of the compression, flexural and round panel tests.

Table 4. Content of fibres in the notched plane of SFRC beam bending tests, and the theoretical content of fibres.

Table 5. Average values of the tensile properties of the steel bars forming the flexural reinforcement of the slabs.

Table 6. Main results obtained in the punching tests.

Table 7. Relevant strain results on the SG_C1.

Table 8. Values of r_y/r_s.

Table 9. Load level at the formation of the first radial and circumferential crack.

Table 10. Data defining the geometry of the failure surface (see Figure 13).

Table 11. Results obtained by applying the developed formulations.

Table 12. Content of fibres determined is cores extracted from the tested slabs.

Table 1. Characteristics of the experimental program.

Series	$d^{(1)}$	ρ	$f_{cm}^{(2)}$	$C_f^{(3)}$
	(mm)	(%)	(MPa)	(kg/m^3)
C_f0f_c50	126	0.85	50	0
C_f0f_c70	130	0.80	70	0
C_f60f_c50	122	0.89	50	60
C_f60f_c70	133	0.77	70	60
C_f75f_c50	129	0.81	50	75
C_f75f_c70	128	0.82	70	75
C_f90f_c50	118	0.95	50	90
C_f90f_c70	117	0.96	70	90

(1) Internal arm of the flexural reinforcement measured after slabs have been tested; Values of: (2) average concrete compressive strength and (3) fiber content, ordered to the ready mix plant company

Table 2. Concrete compositions for the slabs of the experimental program.

Constituent	Series							
	C_f0f_c50	C_f60f_c50	C_f75f_c50	C_f90f_c50	C_f0f_c70	C_f60f_c70	C_f75f_c70	C_f90f_c70
Cement	420	420	420	420	480	480	480	480
Fly ash	65	65	75	80	65	65	75	80
Coarse aggregate (D_{max}=12 mm)	670	668	661	657	628	627	620	619
Coarse Sand	806	804	795	790	757	755	746	741
Fine sand	269	268	265	265	253	252	249	247
Superplasticizer	6.79	7.76	7.92	8.00	7.63	8.72	8.88	8.96
Water	165	165	168	170	185	185	189	190
Fibres	0	60	75	90	0	60	75	90

Table 3. Average values of the compression, flexural and round panel tests.

Series	Age (days)	Compression tests		Three point notched beam bending tests						Round panel test	
		$f_{cm,exp}$ (MPa)	$\varepsilon_{cp,exp}$ (‰)	$f_{fct,L}$ (MPa)	$f_{R,1}$ (MPa)	$f_{R,2}$ (MPa)	$f_{R,3}$ (MPa)	$f_{R,4}$ (MPa)	f_{Ftu} (MPa)	$F_{RPT,max}$ (kN)	$U_{RPT,40}$ (J)
C_f0f_c50	65	57.61 (0.90)	3.04 (2.65)	5.16 (6.71)	-	-	-	-	-	54.07 (-)	-
C_f60f_c50	43	51.90 (6.49)	3.54 (1.83)	3.55 (10.77)	5.71 (20.93)	4.55 (19.50)	2.77 (21.79)	2.13 (29.86)	1.17	48.25 (5.16)	295 (8.63)
C_f75f_c50	52	55.68 (3.91)	4.01 (7.02)	4.27 (5.97)	6.32 (23.89)	5.42 (18.07)	3.25 (23.01)	2.19 (31.48)	1.35	39.00 (4.92)	255 (20.39)
C_f90f_c50	57	56.39 (4.38)	4.41 (11.78)	4.04 (9.93)	11.02 (15.36)	13.62 (16.29)	12.61 (21.08)	10.83 (25.29)	4.44	51.02 (3.99)	813 (11.96)
C_f0f_c70	63	62.63 (0.72)	3.28 (1.71)	4.43 (14.49)	-	-	-	-	-	56. 81 (-)	-
C_f60f_c70	52	63.77 (-)	3.36 (-)	4.64 (9.99)	9.06 (13.35)	9.58 (10.69)	8.08 (14.34)	6.96 (17.46)	2.97	42.55 (8.00)	730 (17.23)
C_f75f_c70	66	70.02 (0.88)	3.35 (1.94)	6.00 (6.62)	12.30 (13.45)	13.30 (11.73)	11.55 (16.07)	10.23 (19.31)	4.20	51.61 (3.32)	829 (11.72)
C_f90f_c70	46	57.63 (2.17)	3.85 (4.77)	4.21 (6.27)	10.51 (24.11)	13.38 (20.98)	11.99 (24.77)	11.04 (31.02)	4.23	49.90 (-)	828 (-)

Table 4. Content of fibres in the notched plane of SFRSCC beam bending tests, and the theoretical content of fibres.

Series	Depth of the notched cross section (mm)	Nº of fibres (N_f)	Fibres per unit area (cm^2)	Theoretical estimation of the content of fibres (Kg/m^3)
C_f60f_c50	125	166	0.89	30
C_f60f_c70	125	295	1.58	53
C_f75f_c50	107.5	155	0.96	32
C_f75f_c70	107.5	416	2.58	86
C_f90f_c50	90	305	2.26	76
C_f90f_c70	90	317	2.34	79

Table 5. Average values of the tensile properties of the steel bars forming the flexural reinforcement of the slabs.

Diameter (mm)	ε_{sy} (‰)	f_{sy} (MPa)	ε_{su} (‰)	f_{su} (MPa)	E_s (GPa)
12	2.53	530	-	684	209.49

Table 6. Main results obtained in the punching tests.

Slab	P_{max} (kN)	δ_{Pmax} (mm)	$P_{max}^{SFRC}/P_{max}^{REF}$	$\delta_{max}^{SFRC}/\delta_{max}^{REF}$	Failure mode
C_f0f_c50	409.11	26.58	-	-	Punching
C_f60f_c50	386.08	28.23	0.94	1.06	Punching
C_f75f_c50	408.03	27.56	1.00	1.04	Punching
C_f90f_c50	456.53	45.81	1.12	1.72	Bending
C_f0f_c70	399.15	25.09	-	-	Punching
C_f60f_c70	462.03	38.63	1.16	1.54	Bending
C_f75f_c70	496.34	48.79	1.24	1.94	Bending
C_f90f_c70	495.58	50.77	1.24	2.02	Bending/Punching

Table 7. Relevant strain results on the SG_C1.

Slab	P_{max} (kN)	$\varepsilon_{c1,Pmax}$ (‰)	$P_{\varepsilon c1,max}$ (kN)	$\varepsilon_{c1,max}$ (‰)	$P_{\varepsilon c1,min}$ (kN)	$\varepsilon_{c1,min}$ (‰)	$\frac{\delta_{\varepsilon c1,max}}{\delta_{P\,max}}$	$\frac{\delta_{\varepsilon c1,min}}{\delta_{P\,max}}$
C_f0f_c50	409.11	0.11	384.03	0.16	-	-	0.85	-
C_f60f_c50	386.08	0.55	369.64	0.76	369.64	-0.03	0.68	1.08
C_f75f_c50	408.03	0.44	369.95	0.65	-*	-*	0.69	-*
C_f90f_c50	456.53	0.12	437.76	0.92	453.40	-0.12	0.54	1.15
C_f0f_c70	399.15	0.03	354.49	0.39	398.80	-0.01	0.66	1.03
C_f60f_c70	462.03	0.32	425.60	0.97	408.58	-0.19	0.55	-**
C_f75f_c70	496.34	-0.07	493.10	0.93	493.10	-0.14	0.67	1.01
C_f90f_c70	495.58	0.09	463.23	0.67	492.18	-0.33	0.65	1.04

*Always compressive strains were registered;
** Not available.

Table 8. Values of r_y/r_s.

Author	Slab's designation	Load level	Failure mode	r_s (mm)	r_y (mm)	r_y/r_s
Reference slabs						
Present study	C_f0f_c50	$0.8 \cdot P_{max}$	Punching	1275	205.6	0.16
	C_f0f_c70	P_{max}	Punching	1275	379.9	0.30
SFRC slabs						
Author	Slab's designation	Load level	Failure mode	r_s (mm)	r_y (mm)	r_y/r_s
Present study	C_f60f_c50	P_{max}	Punching	1275	383.0	0.30
	C_f75f_c50	P_{max}	Punching	1275	200.6	0.16
	C_f90f_c50	$0.9 \cdot P_{max}$	Bending	1275	631.1	0.49
Mcharg [23]	FRSU	P_{max}	Punching	1150	603.8	0.53
	FRSB	P_{max}	Punching	1150	476.5	0.41
Azevedo [24]	HSC.S3	P_{max}	Punching	580	102.0	0.18
Cheng and Parra-Montesinos [25]	S5	P_{max}	Punching	762	265.5	0.37
	S6	P_{max}	Bending/Punching	762	276.7	0.36
	S7	P_{max}	Punching	762	213.0	0.35
	S8	P_{max}	Bending/Punching	762	283.0	0.37
	S9	P_{max}	Punching	762	313.6	0.41
	S10	P_{max}	Bending/Punching	762	284.4	0.55
					Average	0.37
					STD	0.12
					CoV (%)	32.41

Table 9. Load level at the formation of the first radial and circumferential crack.

Slab’s designation	Load level at 1st radial crack	Load level at 1st circumferential crack
C_f0f_c50	$0.31 \cdot P_{max}$	$0.80 \cdot P_{max}$
C_f0f_c70	$0.29 \cdot P_{max}$	$0.81 \cdot P_{max}$
C_f60f_c50	$0.38 \cdot P_{max}$	$[0.66 \cdot P_{max} - 0.86 \cdot P_{max}]$
C_f60f_c70	$0.28 \cdot P_{max}$	$0.86 \cdot P_{max}$
C_f75f_c50	$0.34 \cdot P_{max}$	$0.82 \cdot P_{max}$
C_f75f_c70	$0.24 \cdot P_{max}$	$0.81 \cdot P_{max}$
C_f90f_c50	$0.31 \cdot P_{max}$	$0.79 \cdot P_{max}$
C_f90f_c70	$0.18 \cdot P_{max}$	$0.67 \cdot P_{max}$

Table 10. Data defining the geometry of the failure surface (see Figure 13).

Slab's designation	$r_{0,c}$ (mm)	$r_{0,avg}$ (mm)	θ_{avg} (degrees)	Punching cone formation
C_f0f_c50	0	295 ($1.5 \cdot d$) [(1)]	36	Yes
C_f0f_c70	0	245 ($1.1 \cdot d$) [(1)]	38	Yes
C_f60f_c50	0	240 ($1.15 \cdot d$) [(1)]	47	Yes
C_f60f_c70	-	-	-	No
C_f75f_c50	0	305 ($1.6 \cdot d$) [(1)]	35	Yes
C_f75f_c70	-	-	-	No
C_f90f_c50	-	-	-	No
C_f90f_c70	0	206 ($0.9 \cdot d$) [(1)]	40	Yes

[(1)] The value indicated into the round brackets is a multiple of the internal arm of the conventional reinforcement of the slabs, *d*, and the measure is executed from the perimeter of the loaded area.

Table 11. Results obtained by applying the developed formulations.

Slab	m_R (kN·mm)		$E \cdot I_1$ ($N \cdot mm^2$)		$P_{max}^{exp} / P_{max}^{the}$	
	Simplified	*Refined*	*Simplified*	*Refined*	*Simplified*	*Refined*
C_f60f_c50	70022.26	63678.97	1561345231	2139822311	0.88	0.93
C_f75f_c50	71772.75	64880.790	1720275422	2431392725	0.84	0.90
C_f90f_c50	76597.64	69018.169	1491999468	2016978717	0.85	0.95
C_f60f_c70	77050.59	71062.793	1835064964	2690436074	0.86	0.93
C_f75f_c70	79832.28	72861.609	1734162328	2551984131	0.89	0.98
C_f90f_c70	75127.60	68762.583	1489190271	2032446802	0.95	1.03
				Average	0.88	0.95
				STD	0.04	0.05
				CoV (%)	4.38	4.83

Table 12. Content of fibres determined in cores extracted from the tested slabs.

Slab	Cylinder	Position (mm) [(1)]		C_f (Kg/m^3)					
		In x direction	In y direction	Cylinder		Slab	Slice		
							Top	*Interm.*	*Bottom*
	C1	-980	-615	C1	31.51				
C_f60f_c50	C2	-720	-1085	C2	30.73	29.58	27.66	28.08	32.99
	C3	-1050	855	C3	26.50				
	C1	-815	-1040	C1	54.52				
C_f60f_c70	C2	775	-1030	C2	65.95	59.34	55.14	62.98	59.60
	C3	-1085	-1040	C3	57.55				
	C1	-675	650	C1	44.49				
C_f75f_c50	C2	645	780	C2	30.46	36.45	22.76	37.19	49.40
	C3	945	1070	C3	34.40				
	C1	985	1080	C1	66.40				
C_f75f_c70	C2	745	1070	C2	68.36	67.74	57.57	66.74	78.90
	C3	-1095	970	C3	68.45				
	C1	-955	-1070	C1	99.94				
C_f90f_c50	C2	-705	-1080	C2	103.22	100.86	68.83	110.80	122.96
	C3	655	1080	C3	99.44				
	C1	1135	-920	C1	96.51				
C_f90f_c70	C2	695	-970	C2	97.59	93.92	80.91	91.64	109.21
	C3	-985	-1070	C3	87.66				

[(1)] The coordinates of the centre of the cylinder are referred to the centre of the slab.

LIST OF FIGURE CAPTIONS

Figure 1. Geometry of the slab prototype (dimensions in mm).

Figure 2. Flexural reinforcement in: a) reference slabs, b) SFRC slabs; Cross section of c) AA, and d) BB (dimensions in mm).

Figure 3. Test setup: a) Top view, b) Bottom view.

Figure 4. Applied monitoring system: a) position of the LVDTs, b) position of the strain gauges in the steel bars, and c) position of the strain gauges in the concrete bottom surface (dimensions in mm).

Figure 5. Average curves of the flexural stress-CMOD of the SFRC three point notched beam bending tests.

Figure 6. Results from the round panel tests: a) and b) Force-deflection in the series of f_{cm}=50 MPa and f_{cm}=70 MPa, respectively; c) and d) Energy-deflection in the series of f_{cm}=50 MPa and f_{cm}=70 MPa, respectively.

Figure 7. Force-centre deflection in the tested series of slabs of target average compressive strength of: a) 50 MPa, b) 70 MPa.

Figure 8. Relationship between P_{max} and: a) $f_{R,1}$; b) $f_{R,2}$; c) $f_{R,3}$; d) $f_{R,4}$; e) $U_{RPT,40}$; f) f_{ftu}

Figure 9. Load-strain in SG_C1 for the series of slabs: a) f_{cm}=50 MPa, and b) f_{cm}=70 MPa.

Figure 10. Concept of r_y: boundary corresponding to the yield initiation of flexural reinforcement.

Figure 11. Crack pattern in the top surface for the slabs: a) C_f0f_c50, b) C_f0f_c70, c) C_f60f_c50, d) C_f60f_c70, e) C_f75f_c50, f) C_f75f_c70, g) C_f90f_c50, h) C_f90f_c70.

Figure 12. Internal failure surface of the slabs: a) C_f0f_c50, b) C_f0f_c70, c) C_f60f_c50, d) C_f60f_c70, e) C_f75f_c50, f) C_f75f_c70, g) C_f90f_c50, h) C_f90f_c70.

Figure 13. Parameters adopted to define the punching failure surface.

Figure 14. a) Assumed crack pattern in a column-slab connection, b) Stresses and resultant forces in a radial segment of the slab, and c) 2L and 4L moment curvature (m-χ) diagrams.

Figure 15. Adopted approach to evaluate the ultimate bending moment, m_R (adapted from the *fib* Model Code 2010 [11]).

Figure 16. Relationship between ψ and (V/V_{flex}) for: a) f_c50, and b) f_c70.

Figure 17. V-ψ relationship for the slabs: a) C_f60f_c50, b) C_f75f_c50, c) C_f90f_c50, d) C_f60f_c70, e) C_f75f_c70, e f) C_f90f_c70.

Figure 18. Cross section layer model applied to the tested slabs.

Figure 19. Constitutive laws of the tensile behaviour of the SFRSCC adopted on the cross section layer model for: a) C_f60f_c50, b) C_f75f_c50, c) C_f90f_c50, d) C_f60f_c70, e) C_f75f_c70, e f) C_f90f_c70.

Figure 20. Moment-curvature relationship obtained from the cross section layer model for: a) f_{cm}=50 MPa, and b) f_{cm}=70 MPa.

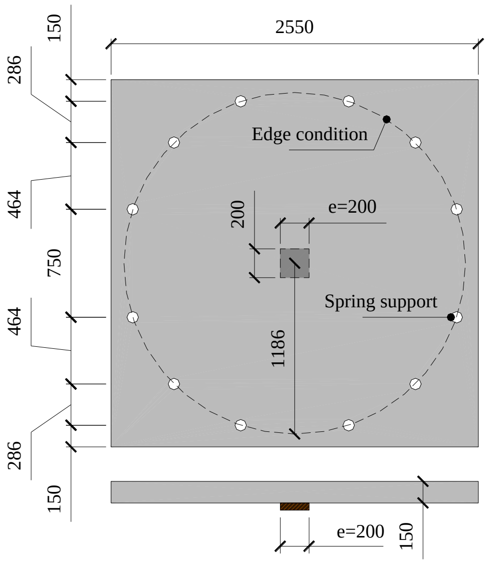

Figure 1. Geometry of the slab prototype (dimensions in mm).

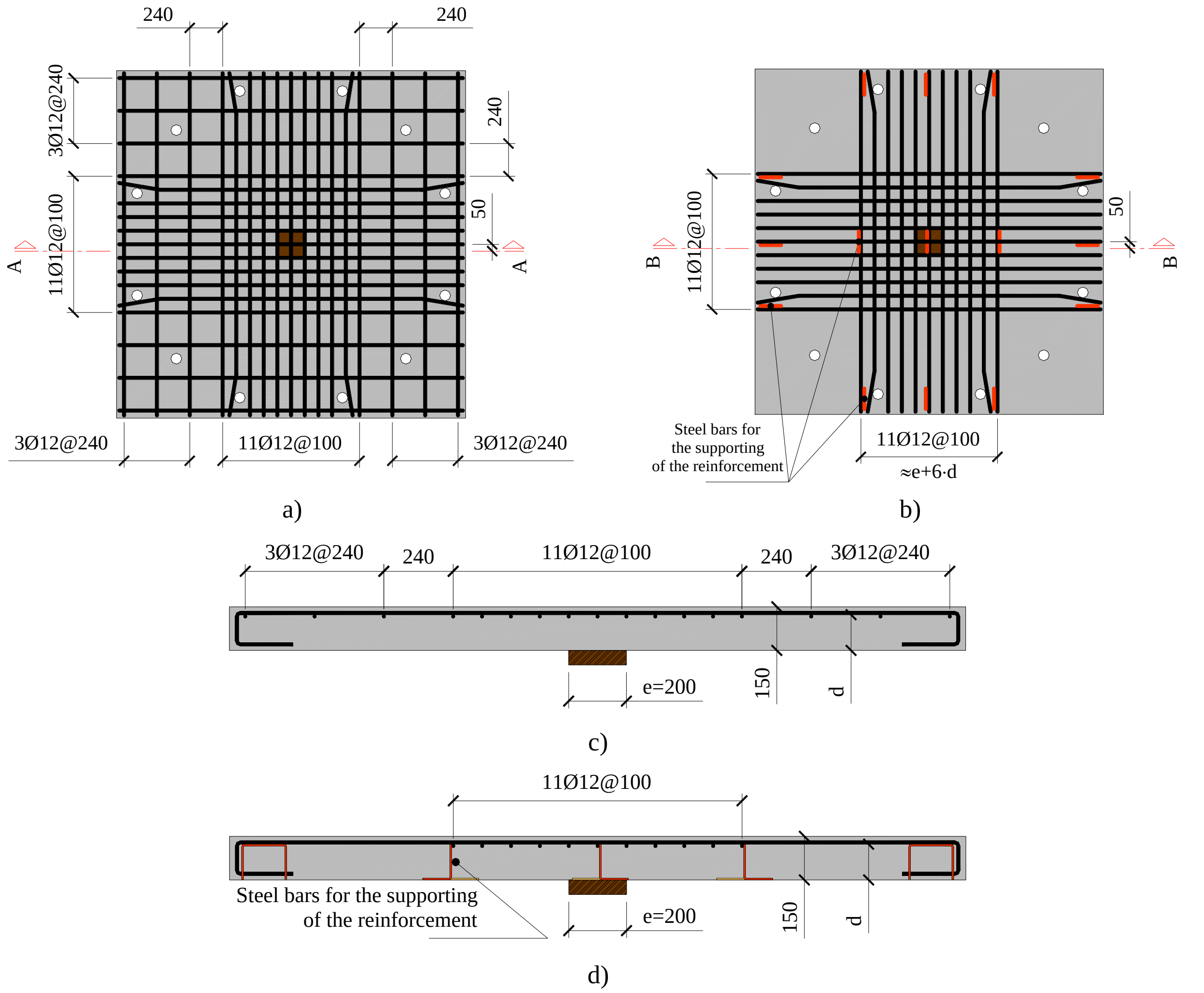

Figure 2. Flexural reinforcement in: a) reference slabs; b) SFRSCC slabs; Cross section of c) AA, and d) BB (dimensions in mm).

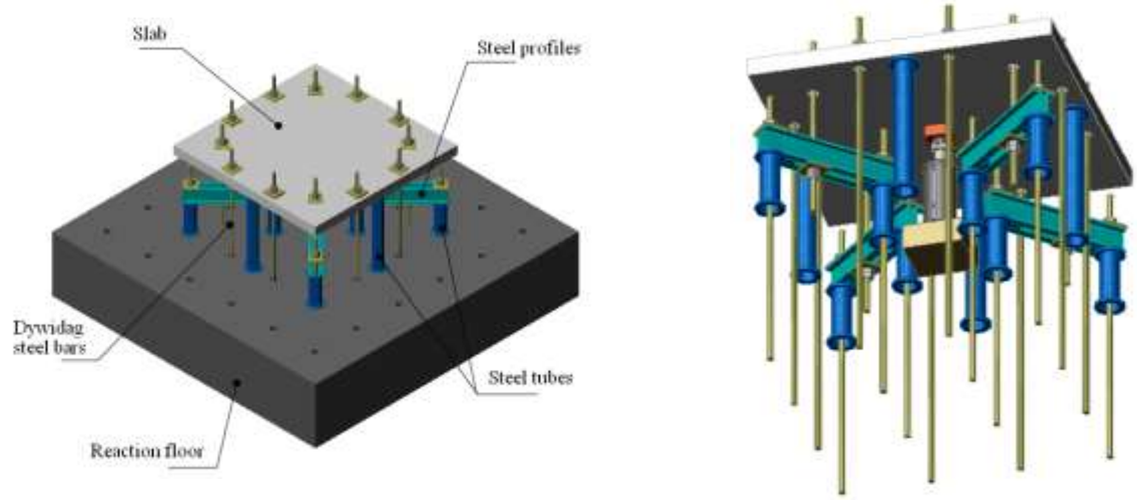

a) b)

Figure 3. Test setup: a) Top view, b) Bottom view.

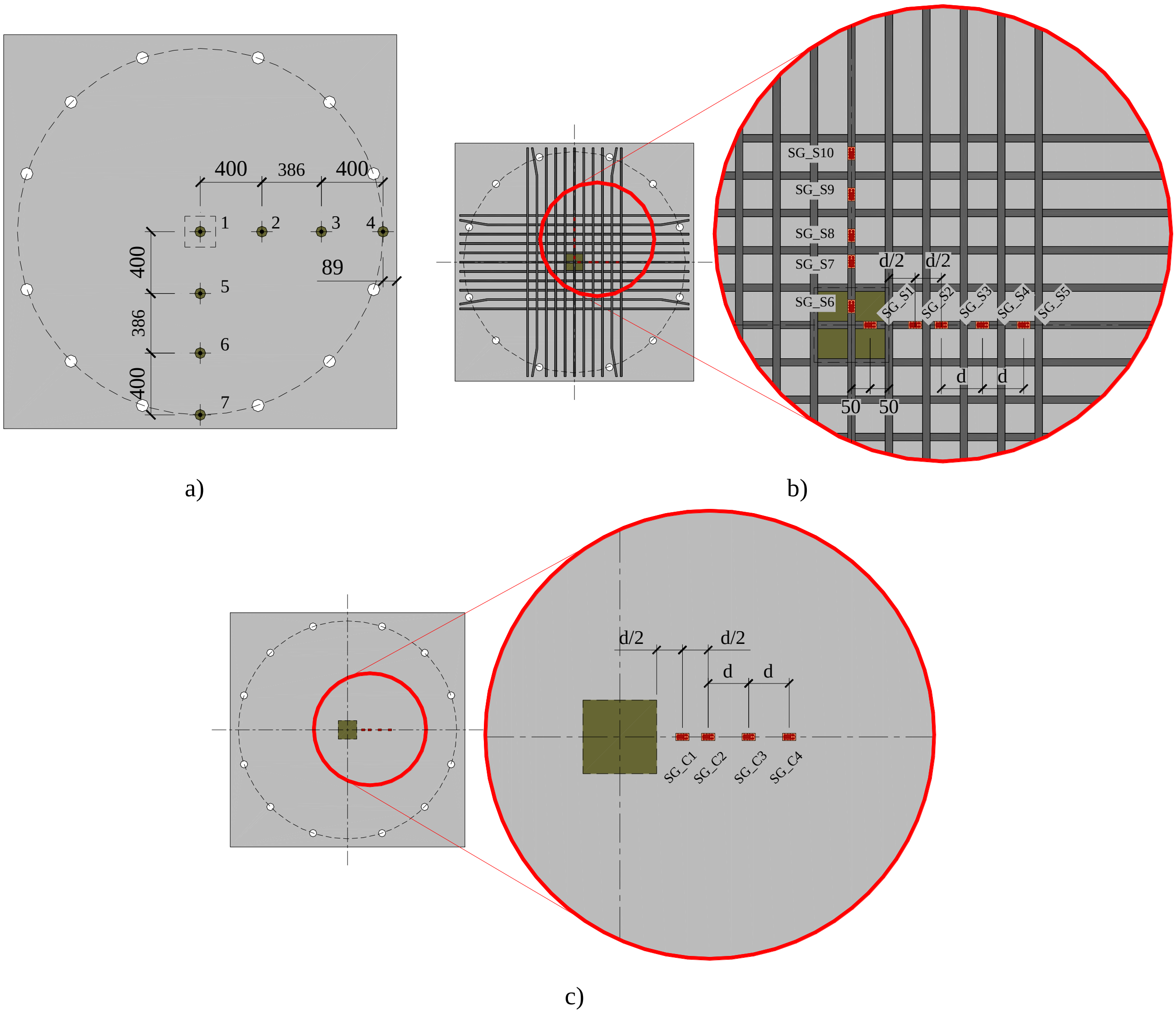

Figure 4. Applied monitoring system: a) position of the LVDTs, b) position of the strain gauges in the steel bars, and c) position of the strain gauges on the concrete bottom surface (dimensions in mm).

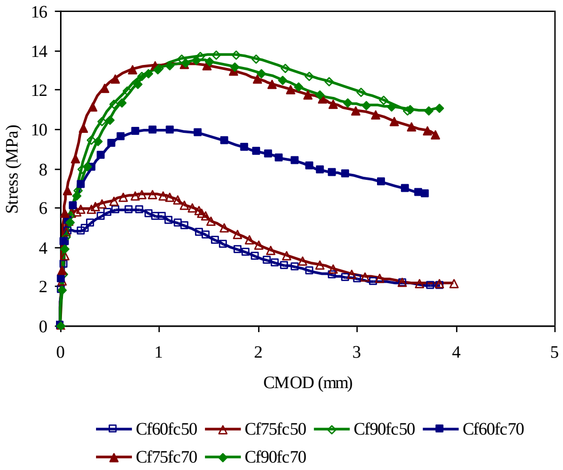

Figure 5. Average curves of the flexural stress-CMOD of the three point notched SFRSCC beam bending tests.

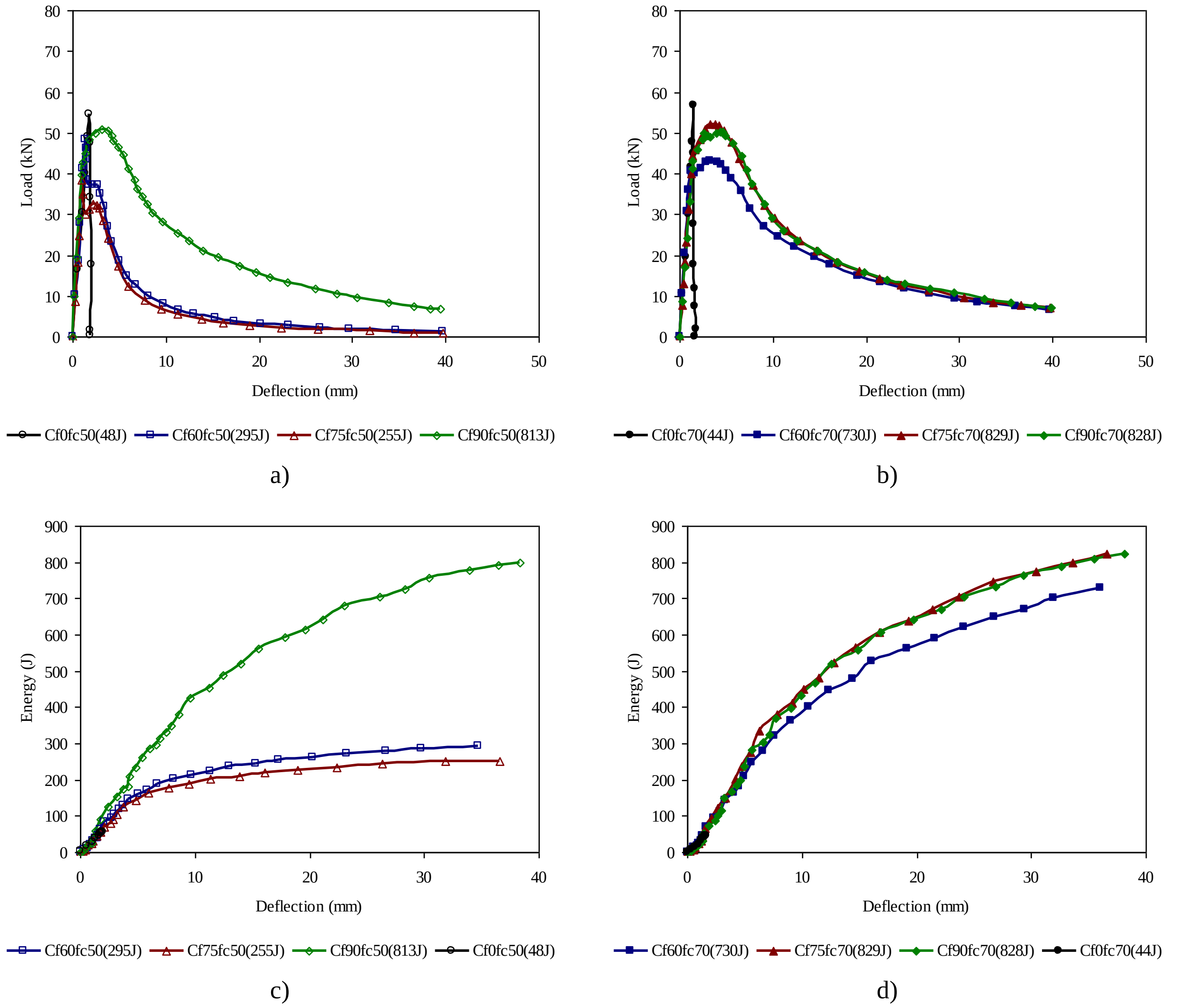

Figure 6. Results from the round panel tests: a) and b) Force-deflection in the series of f_{cm}=50 MPa and f_{cm}=70 MPa, respectively; c) and d) Energy-deflection in the series of f_{cm}=50 MPa and f_{cm}=70 MPa, respectively.

732

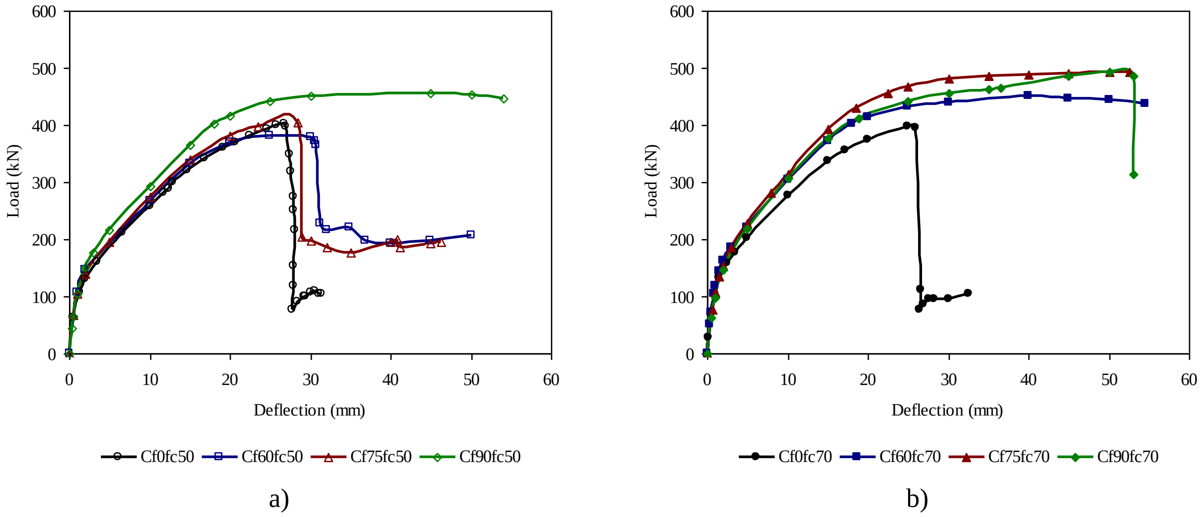

Figure 7. Force-centre deflection in the tested series of slabs of target average compressive strength of: a) 50 MPa, b) 70 MPa.

733

734

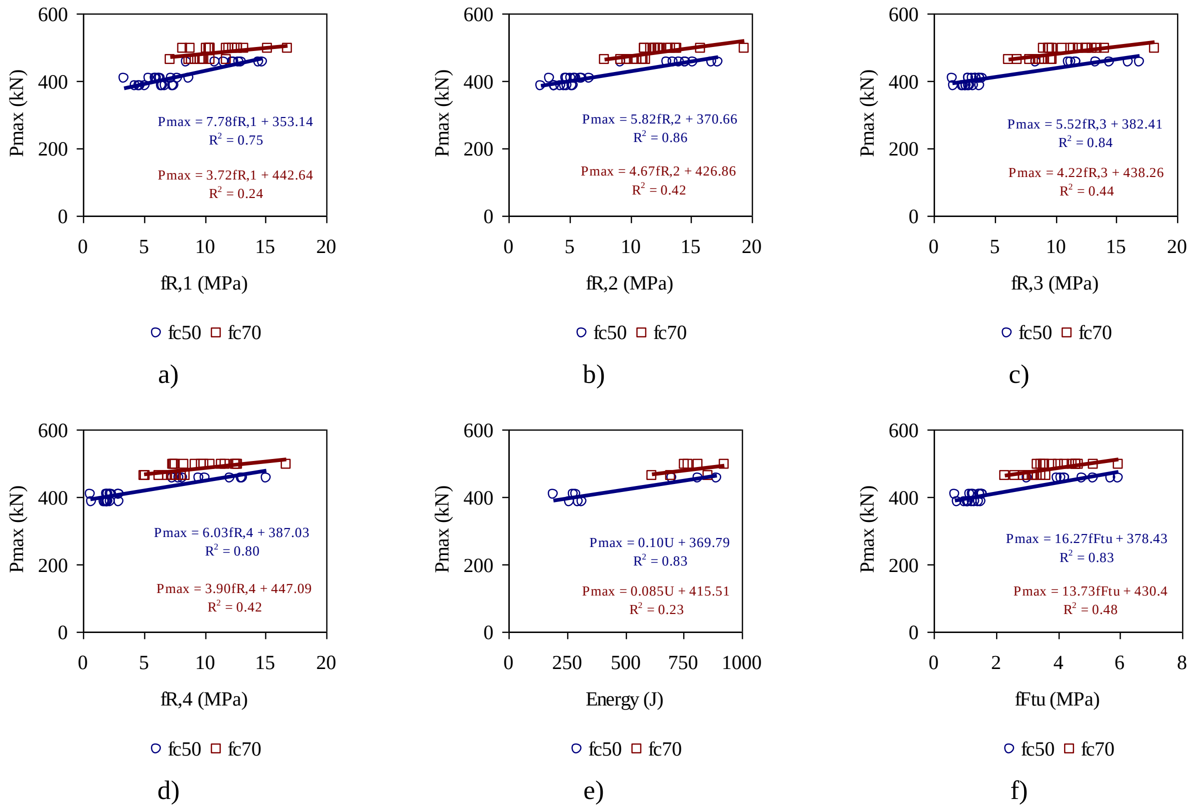

Figure 8. Relationship between P_{max} and: a) $f_{R,1}$; b) $f_{R,2}$; c) $f_{R,3}$; d) $f_{R,4}$; e) $U_{RPT,40}$; f) f_{ftu}.

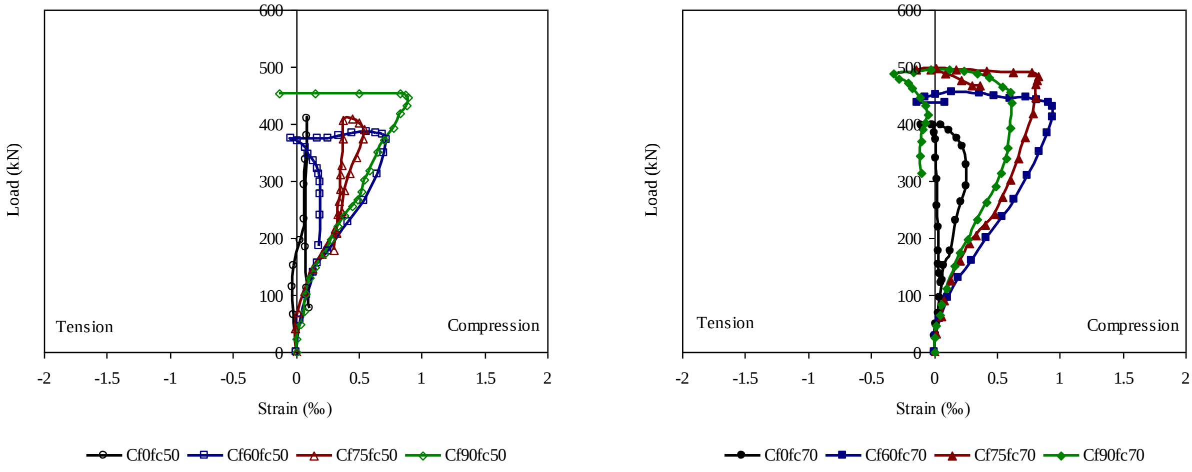

a) b)

Figure 9. Load-strain in SG_C1 for the series of slabs: a) f_{cm}=50 MPa, and b) f_{cm}=70 MPa.

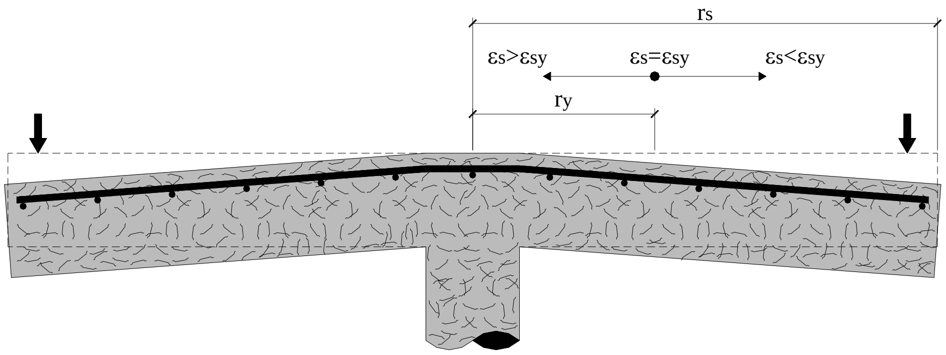

Figure 10. Concept of r_y: boundary corresponding to the yield initiation of flexural reinforcement.

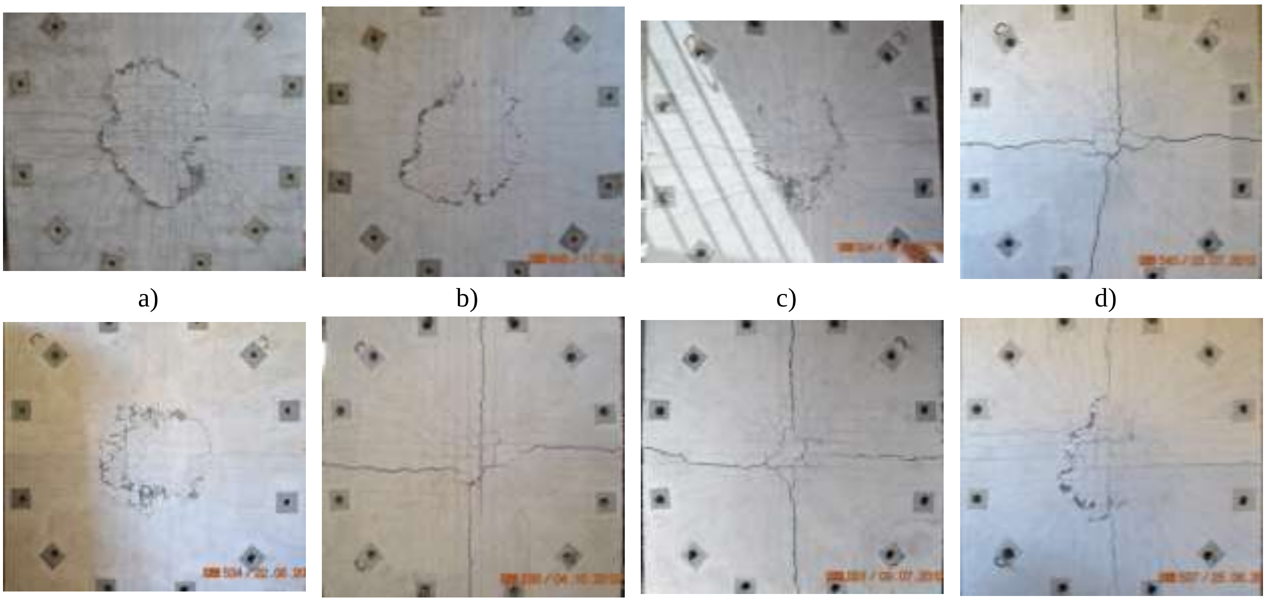

a) b) c) d) e) f) g) h)

Figure 11. Crack pattern in the top surface for the slabs: a) C_f0f_c50, b) C_f0f_c70, c) C_f60f_c50, d) C_f60f_c70, e) C_f75f_c50, f) C_f75f_c70, g) C_f90f_c50, h) C_f90f_c70.

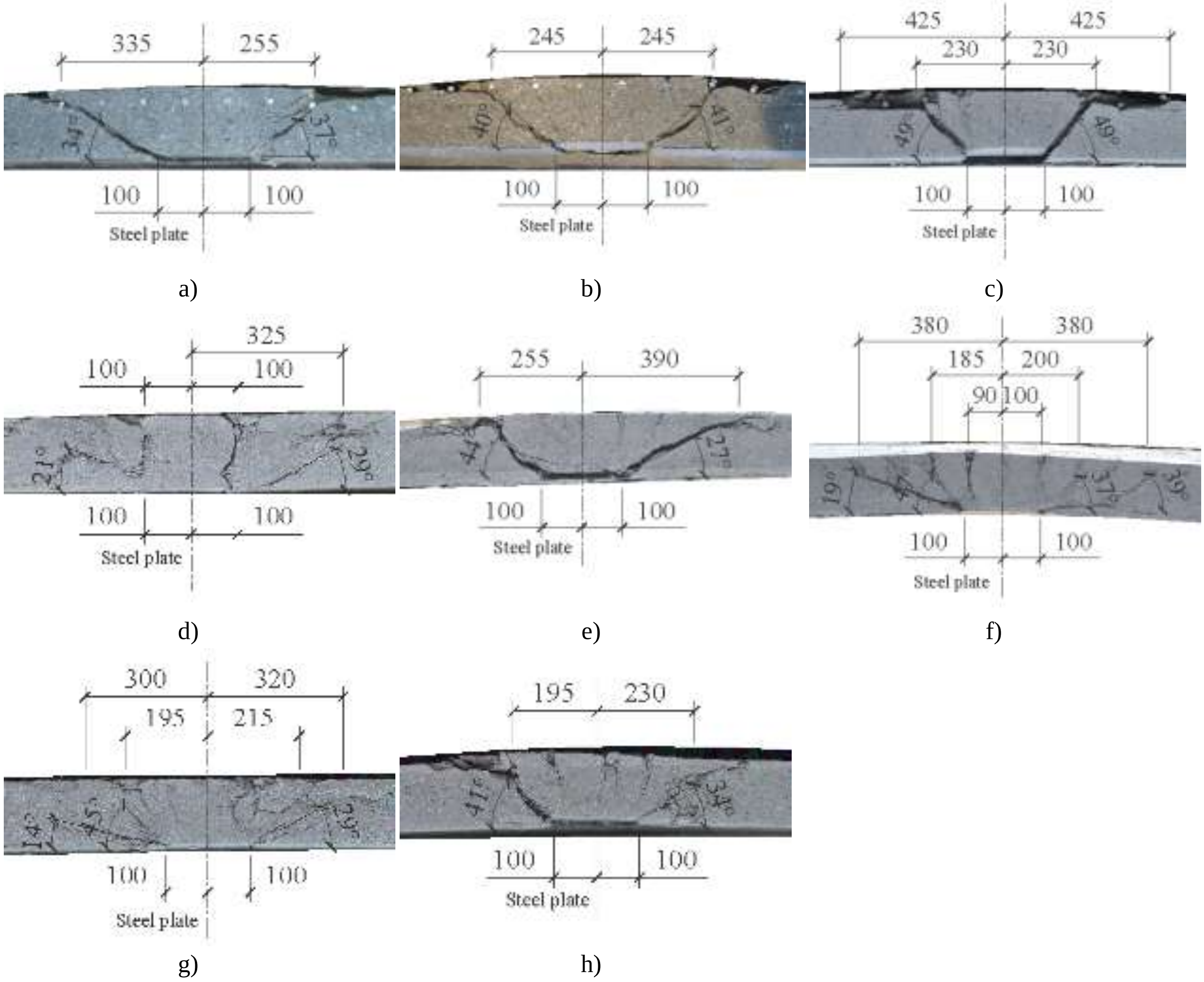

Figure 12. Internal failure surface of the slabs: a) C_f0f_c50, b) C_f0f_c70, c) C_f60f_c50, d) C_f60f_c70, e) C_f75f_c50, f) C_f75f_c70, g) C_f90f_c50, h) C_f90f_c70.

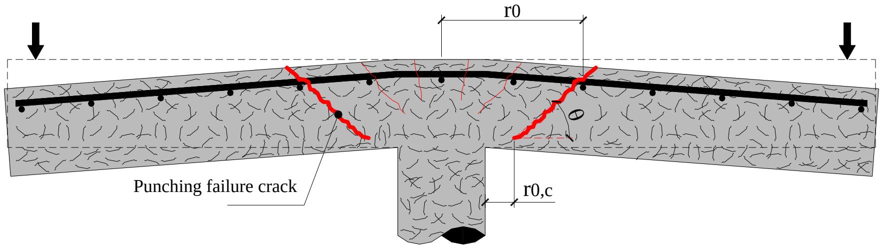

Figure 13. Parameters adopted to define the punching failure surface.

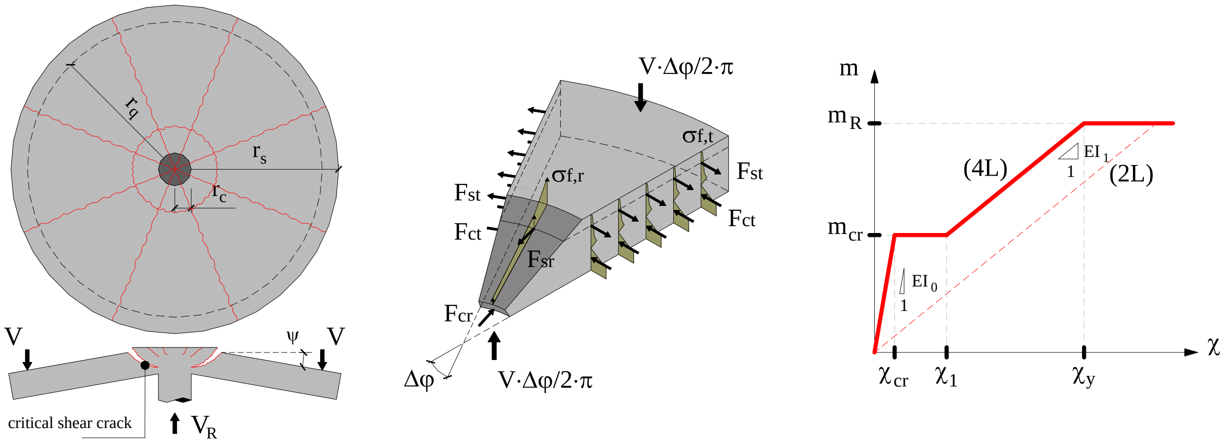

a) b) c)

Figure 14. a) Assumed crack pattern in a column-slab connection, b) Stresses and resultant forces in a radial segment of the slab, and c) 2L and 4L moment curvature (m-χ) diagrams.

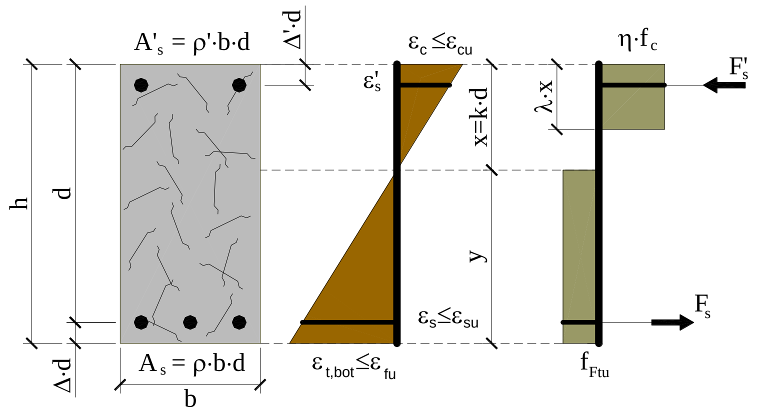

Figure 15. Adopted approach to evaluate the ultimate bending moment, m_R (adapted from the *fib* Model Code 2010 [11]).

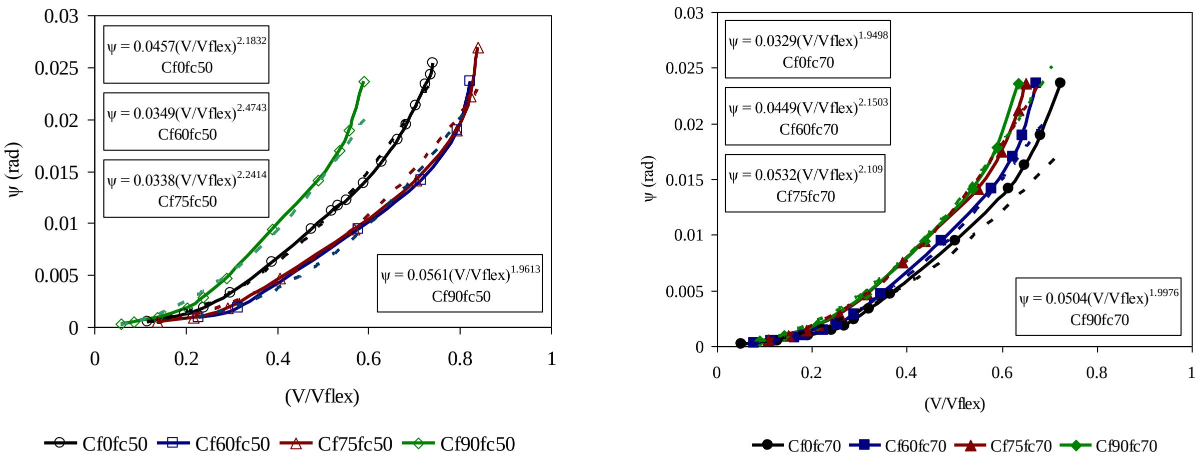

a) b)

Figure 16. Relationship between ψ and (V/V_{flex}) for: a) f_c50, and b) f_c70.

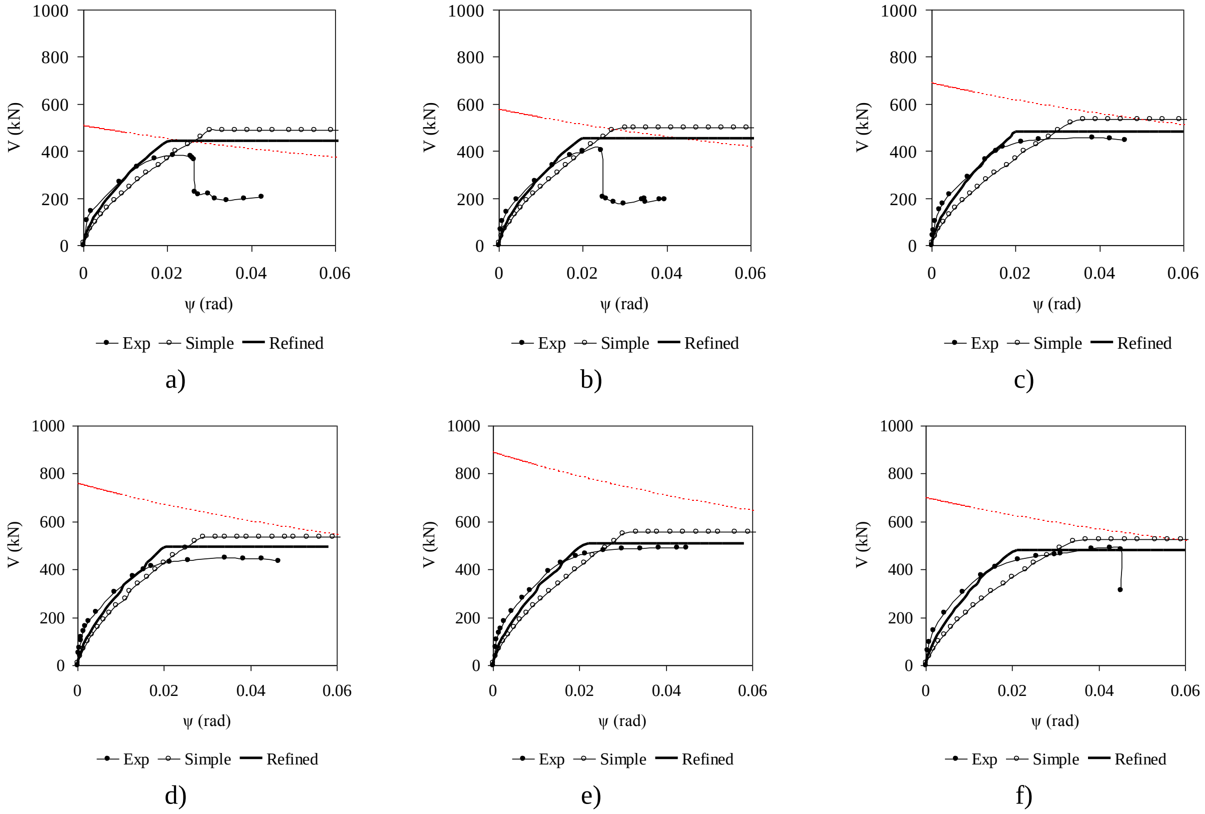

Figure 17. V-ψ relationship for the slabs: a) C_f60f_c50, b) C_f75f_c50, c) C_f90f_c50, d) C_f60f_c70, e) C_f75f_c70, e f) C_f90f_c70.

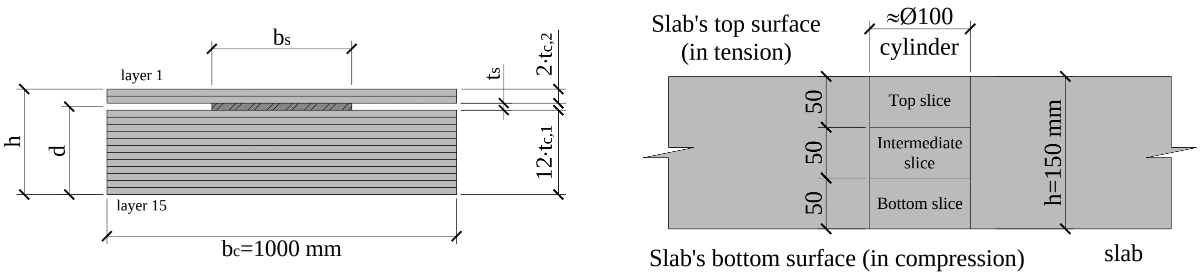

Figure 18. Cross section layer model applied to the tested slabs.

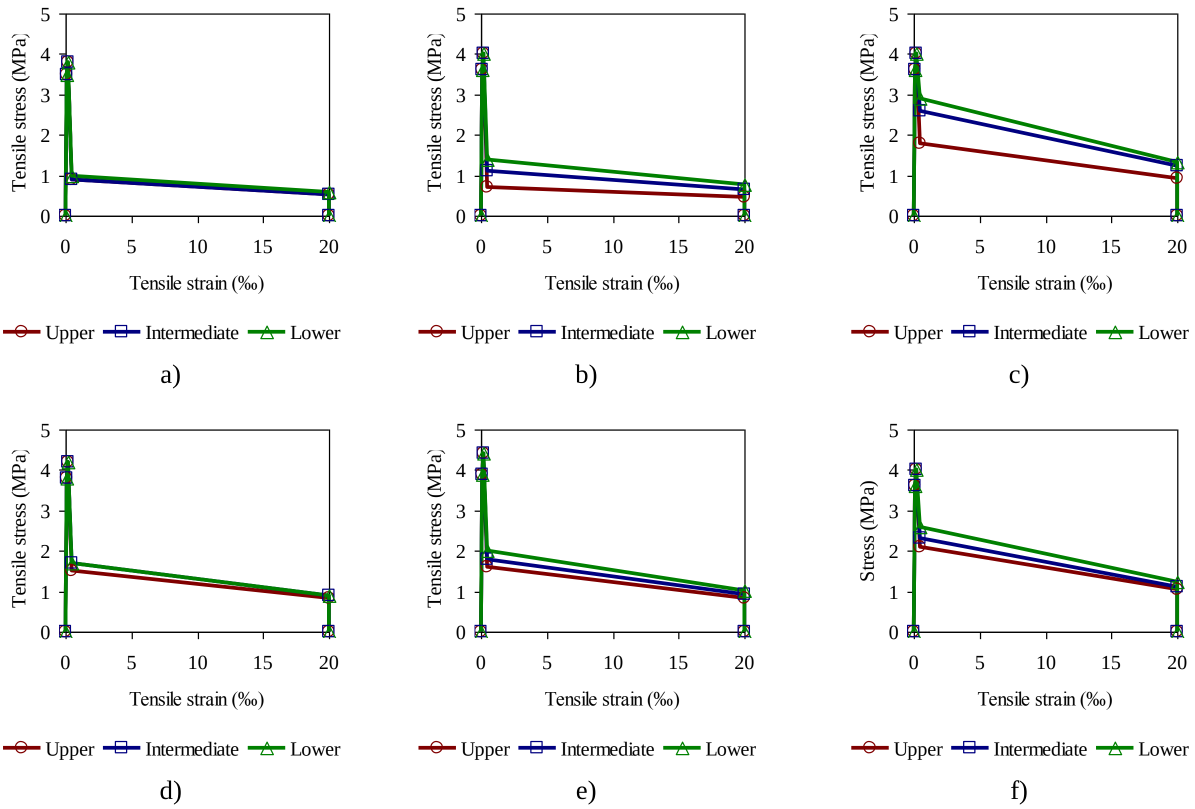

Figure 19. Constitutive laws of the tensile behaviour of the SFRSCC adopted on the cross section layer model for: a) C_f60f_c50, b) C_f75f_c50, c) C_f90f_c50, d) C_f60f_c70, e) C_f75f_c70, e f) C_f90f_c70.

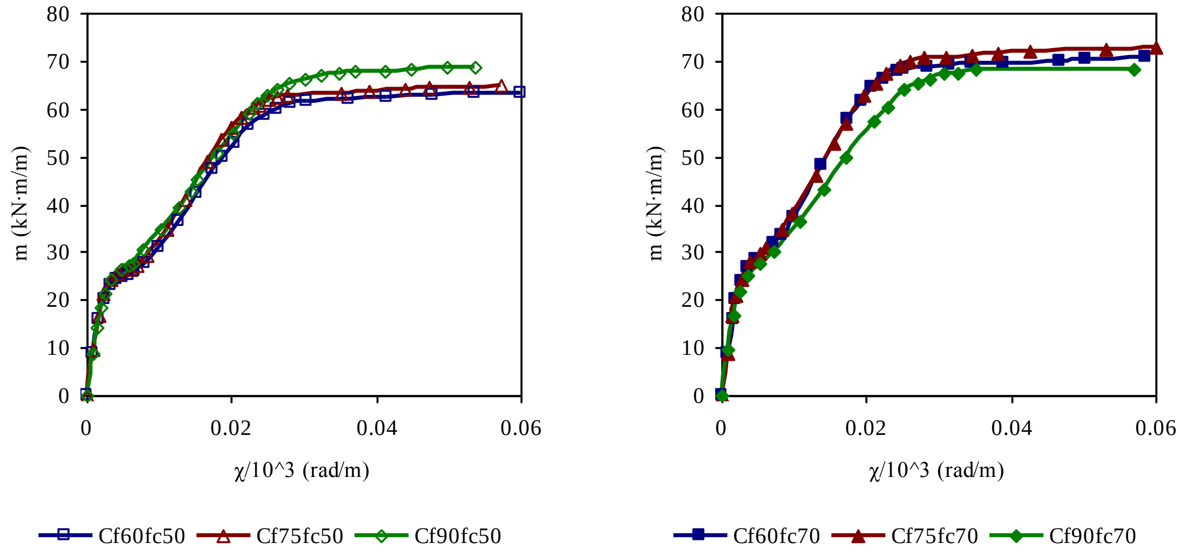

a) b)

Figure 20. Moment-curvature relationship obtained from the cross section layer model: a) f_{cm}=50 MPa, and b) f_{cm}=70 MPa.